



저작자표시-비영리-변경금지 2.0 대한민국

이용자는 아래의 조건을 따르는 경우에 한하여 자유롭게

- 이 저작물을 복제, 배포, 전송, 전시, 공연 및 방송할 수 있습니다.

다음과 같은 조건을 따라야 합니다:



저작자표시. 귀하는 원저작자를 표시하여야 합니다.



비영리. 귀하는 이 저작물을 영리 목적으로 이용할 수 없습니다.



변경금지. 귀하는 이 저작물을 개작, 변형 또는 가공할 수 없습니다.

- 귀하는, 이 저작물의 재이용이나 배포의 경우, 이 저작물에 적용된 이용허락조건을 명확하게 나타내어야 합니다.
- 저작권자로부터 별도의 허가를 받으면 이러한 조건들은 적용되지 않습니다.

저작권법에 따른 이용자의 권리는 위의 내용에 의하여 영향을 받지 않습니다.

이것은 [이용허락규약\(Legal Code\)](#)을 이해하기 쉽게 요약한 것입니다.

[Disclaimer](#)

공학박사 학위논문

**Controlling In-Plane Cation Ordering for High
Reversibility in Layered Oxide Cathodes of
Sodium Ion Battery**

소듐 이온 배터리 층상구조 양극 물질의 높은 가
역성을 위한 양이온 배열 조절에 관한 연구

2020 년 2 월

서울대학교 대학원

공과대학 화학생물공학부 에너지환경화학융합기술전공

강 석 문

Abstract

Controlling In-Plane Cation Ordering for High Reversibility in Layered Oxide Cathodes of Sodium Ion Battery

Seok Mun Kang

School of Chemical and Biological Engineering

Chemical Convergence for Energy & Environment

The Graduate School

Seoul National University

Lithium ion batteries (LIBs) have been widely used as power sources for portable electronics such as laptop and mobile phone for the past few decades. Owing to growing concern about environmental issues, LIBs are now considered one of the most credible power sources for large scale energy storage applications such as electric vehicle (EV) and energy storage system (ESS). However, uneven distribution of lithium resources and rising cost of lithium hinder the rapid growth of the large-scale LIBs market. Therefore, the alternatives to the LIBs have attracted much attention in recent years.

Sodium ion batteries (SIBs) are regarded as promising candidates for the LIB alternatives because sodium resources are earth-abundant and cost-effective compared to lithium resources. Additionally, SIBs share the same electrochemistry

and basic principles with LIBs, which enable SIBs to exploit the-state-of-the art technology built up in LIBs. Despite these advantages of SIBs, SIBs suffer from insufficient energy densities, which hinder their commercialization because Na ion is larger and heavier than Li ion and Na has a higher standard electrode potential than that of Li. In this regard, advancement of electrode materials is required to overcome low energy densities from the intrinsic properties of Na. Especially, search for high-voltage cathode electrode materials is a major research topic because a cathode electrode material determines the net operating voltage of SIB cell.

In chapter 1, general information for SIBs is introduced based on differences between LIBs and SIBs. And, P2-type layered transition metal oxides are introduced with brief demonstration of the P2-type layered structure, which are promising high-capacity cathode electrode materials. In addition, three types of ordering in P2-type layered structure are explained because they are important microstructure, which can affect the electrochemical performance.

In chapter 2, improved electrochemical performance of P2-type $\text{Na}_{0.67}\text{Co}_{0.90}\text{Ti}_{0.10}\text{O}_2$ is discussed in comparison with P2-type $\text{Na}_{0.67}\text{CoO}_2$. P2-type $\text{Na}_{0.67}\text{CoO}_2$ suffers from severe phase transitions caused by Na^+ /vacancy ordering, which affect capacity retention and rate capability. In addition, utilization of Na ion is limited due to irreversible phase transition at high voltage region. To solve these phase transition issues, Ti^{4+} ion is partially introduced instead of Co^{4+} ion because Ti^{4+} ion is expected to disorder cation ordering between Co^{3+} and Ti^{4+} due to its comparable ionic radii and disorder charge ordering between Co^{3+} and Co^{4+} , which is coupled with the Na^+ /vacancy ordering. As Na^+ /vacancy ordering is mitigated in P2-type $\text{Na}_{0.67}\text{CoO}_2$, irreversible phase change in high voltage region is mitigated in

addition to the Na⁺/vacancy ordering-related phase transitions in P2-Na_{0.67}Co_{0.90}Ti_{0.10}O₂. Therefore, Na_{0.67}Co_{0.90}Ti_{0.10}O₂ has wider operating voltage window and higher energy density than those of P2-Na_{0.67}CoO₂. From these results, the mitigation of Na⁺/vacancy ordering can have advantages in not only a rate capability or a capacity retention but also an energy density with an extended voltage range in SIB layered transition metal oxide cathode electrode materials.

Keywords: sodium ion batteries, layered oxide cathodes, in-plane cation ordering, reversibility, high-voltage

Student number: 2014-22589

List of Tables

Table 1. 1 Comparison for Lithium and Sodium as charge carrier for rechargeable batteries. Adapted from Ref [6] (N. Yabuuchi, K. Kubota, M. Dahbi, S. Komaba, <i>Chem. Rev.</i> , 2014, <i>114</i> , 11636).	4
Table 1. 2 Disordered/Ordered structure in P2-type layered transition metal oxides $\text{Na}_x[\text{M}_1\text{M}_2]\text{O}_2$. Adapted from Ref [19] (Y. Wang, R. Xiao, Y.-S. Hu, M. Avdeev, L. Chen, <i>Nat. Commun.</i> , 2015, <i>6</i> , 6954).	14
Table 2. 1 Unit cell constants and atomic parameters of P2-type (a) $\text{Na}_{0.67}\text{CoO}_2$, (b) $\text{Na}_{0.67}\text{Co}_{0.95}\text{Ti}_{0.05}\text{O}_2$, and (c) $\text{Na}_{0.67}\text{Co}_{0.90}\text{Ti}_{0.10}\text{O}_2$ samples calculated from Rietveld refinement of SXRD data.	25
Table 2. 2 Selected bond distances, MO_2 slab thickness, and NaO_2 interslab distance of P2-type $\text{Na}_{0.67}\text{CoO}_2$, $\text{Na}_{0.67}\text{Co}_{0.95}\text{Ti}_{0.05}\text{O}_2$, and $\text{Na}_{0.67}\text{Co}_{0.90}\text{Ti}_{0.10}\text{O}_2$ samples calculated from Rietveld refinement of SXRD data.	27
Table 2. 3 Atomic compositions of $\text{Na}_{0.67}\text{Co}_{1-x}\text{Ti}_x\text{O}_2$ ($x = 0, 0.05$ and 0.1) samples confirmed by ICP-AES analysis.	28

List of Figures

- Figure 1. 1** Schematic illustration of the sodium ion batteries. Adapted from Ref [6] (N. Yabuuchi, K. Kubota, M. Dahbi, S. Komaba, *Chem. Rev.*, 2014, *114*, 11636).4
- Figure 1. 2** Comparison of SIB cathode materials in terms of working potential and specific capacity. Adapted from Ref [7] (J.-Y. Hwang, S.-T. Myung, Y.-K. Sun, *Chem. Soc. Rev.*, 2017, *46*, 3529).6
- Figure 1. 3** Structures of SIB layered type transition metal oxide polymorphs. Adapted from Ref [6] (N. Yabuuchi, K. Kubota, M. Dahbi, S. Komaba, *Chem. Rev.*, 2014, *114*, 11636).7
- Figure 1. 4** 1.4 Na diffusion pathway in different SIB layered polymorphs. Adapted from Ref [6] (N. Yabuuchi, K. Kubota, M. Dahbi, S. Komaba, *Chem. Rev.*, 2014, *114*, 11636).9
- Figure 1. 5** Voltage-capacity profile for a Na/P2-Na_{2/3}[Ni_{1/3}Mn_{2/3}]O₂ cell. Adapted from Ref [12] (Z. Lu, J. R. Dahn, *J. Electrochem. Soc.*, 2001, *148*, A1225). ...10
- Figure 1. 6** Voltage-capacity profile for a Na/P2-Na_{2/3}[Fe_{1/2}Mn_{1/2}]O₂ cell. Adapted from Ref [16] (N. Yabuuchi, M. Kajiyama, J. Iwatate, H. Nishikawa, S. Hitomi, R. Okuyama, R. Usui, Y. Yamada, S. Komaba, *Nat. Mater.*, 2012, *11*, 512).12
- Figure 2. 1** (a) Schematic illustration of the P2-type Na_{0.67}Co_{1-x}Ti_xO₂ crystal structure. Two different sites exist for Na; Na1 and Na2. (b) Synchrotron X-ray powder diffraction (SXRPD) patterns of Na_{0.67}Co_{1-x}Ti_xO₂ ($x = 0, 0.05, 0.1, 0.15, \text{ and } 0.2$). The wavelength of the radiation is 1.49150 Å. Inset shows a

peak from an unknown impurity phase near the (002) peak. The asterisks indicate impurity phases. (c) Variations of lattice parameter of a and unit cell volume V with the amount of substituted Ti^{4+} in $\text{Na}_{0.67}\text{Co}_{1-x}\text{Ti}_x\text{O}_2$ ($x = 0, 0.05,$ and 0.1) (d) Enlarged SXRPD patterns of $\text{Na}_{0.67}\text{Co}_{1-x}\text{Ti}_x\text{O}_2$ ($x = 0, 0.05,$ and 0.1) between 26.0° to 32.5° . The blue diamonds indicate superstructure peaks from Na^+ /vacancy ordering22

Figure 2. 2 FE-SEM images of as-synthesized P2-type (a) $\text{Na}_{0.67}\text{CoO}_2$, (b) $\text{Na}_{0.67}\text{Co}_{0.95}\text{Ti}_{0.05}\text{O}_2$, (c) $\text{Na}_{0.67}\text{Co}_{0.90}\text{Ti}_{0.10}\text{O}_2$, and (d) $\text{Na}_{0.67}\text{Co}_{0.85}\text{Ti}_{0.15}\text{O}_2$ powder samples. Scale bar = 5 μm23

Figure 2. 3 Rietveld plots for P2-type (a) $\text{Na}_{0.67}\text{CoO}_2$, (b) $\text{Na}_{0.67}\text{Co}_{0.95}\text{Ti}_{0.05}\text{O}_2$, and (c) $\text{Na}_{0.67}\text{Co}_{0.90}\text{Ti}_{0.10}\text{O}_2$ obtained by refining SXRPD data. The red dots and black solid lines indicate the observed and calculated patterns, respectively. The blue solid lines indicate their difference, and the green tick marks indicate the peak positions of the diffraction.....24

Figure 2. 4 Electrochemical cycling performance of the $\text{Na}/\text{Na}_{0.67}\text{Co}_{1-x}\text{Ti}_x\text{O}_2$ ($x = 0, 0.05,$ and 0.1) cells. (a–c) Galvanostatic charge/discharge curve of $\text{Na}_{0.67}\text{Co}_{1-x}\text{Ti}_x\text{O}_2$ ($x = 0, 0.05,$ and 0.1) during 100 cycles. The test was conducted at 100 mA g^{-1} between 2 and 4.4 V. (d) dQ/dV plots of the 2nd charge/discharge curve from a-c. (e) Specific capacity and Coulombic efficiency of each cell as a function of cycle number. (f) Specific energy of each cell as a function of cycle number.33

Figure 2. 5 (a) Rate performance of the $\text{Na}/\text{Na}_{0.67}\text{Co}_{1-x}\text{Ti}_x\text{O}_2$ ($x = 0, 0.05$ and 0.1) cells. Discharge curves with various current densities for (b) $\text{Na}_{0.67}\text{CoO}_2$ and (c) $\text{Na}_{0.67}\text{Co}_{0.90}\text{Ti}_{0.10}\text{O}_2$, respectively.....35

Figure 2. 6 (a) Galvanostatic intermittent titration technique (GITT) curves of $\text{Na}_{0.67}\text{CoO}_2$ and $\text{Na}_{0.67}\text{Co}_{0.90}\text{Ti}_{0.10}\text{O}_2$. These GITT curves involve a repeated charge at 5 mA g^{-1} for 1 h followed by resting for 2 h. Voltage plots as a function of time for (b) $\text{Na}_{0.67}\text{CoO}_2$ and (c) $\text{Na}_{0.67}\text{Co}_{0.90}\text{Ti}_{0.10}\text{O}_2$38

Figure 2. 7 Electrochemical cycling performance of the $\text{Na}/\text{Na}_{0.67}\text{Co}_{1-x}\text{Ti}_x\text{O}_2$ ($x = 0$ and 0.1) cells, where 100 mA g^{-1} of current density is applied between 2.0 and 4.5 V. (a) Discharge capacity and Coulombic efficiency of each cell as a function of cycle number up to 300 cycles. (b,c) Charge/discharge curves of $\text{Na}_{0.67}\text{CoO}_2$ and $\text{Na}_{0.67}\text{Co}_{0.90}\text{Ti}_{0.10}\text{O}_2$, respectively.....40

Figure 2. 8 Ex situ XRD patterns of (a) $\text{Na}_{0.67}\text{CoO}_2$ and (b) $\text{Na}_{0.67}\text{Co}_{0.90}\text{Ti}_{0.10}\text{O}_2$. For each sample, an electrode discharged after cell assembly and an electrode discharge after 300 cycles were compared.....42

Figure 2. 9 Discharge profile of $\text{Na}_{0.67}\text{CoO}_2$ at a very low current density (2 mA g^{-1}) after 100 charge/discharge cycling in a voltage window 2-4.5 V at 100 mA g^{-1}43

Figure 2. 10 (a),(b) Two different TEM SAED patterns observed from the surface of capacity decayed $\text{Na}_{0.67}\text{CoO}_2$ (after 100 cycles between 2.0 and 4.5 V). (c) Simulated SAED pattern of a zone axis $[0\ 0\ 1]$ of Na_xCoO_2 . (d) Simulated SAED pattern of a zone axis $[1\ 0\ 0]$ of Co_3O_444

Figure 2. 11 TEM SAED patterns observed from the surface of $\text{Na}_{0.67}\text{Co}_{0.90}\text{Ti}_{0.10}\text{O}_2$ after 100cycles between 2.0-4.5 V.46

Figure 2. 12 Transmission in situ XRD patterns (right side) with voltage profiles (left side) of (a) $\text{Na}_{0.67}\text{CoO}_2$ and (b) $\text{Na}_{0.67}\text{Co}_{0.90}\text{Ti}_{0.10}\text{O}_2$ during galvanostatic charging at a rate of 10 mA g^{-1} . The peak is a hexagonal (0 0 2) peak. (c)

Evolution of lattice parameter c for $\text{Na}_{0.67}\text{CoO}_2$ and $\text{Na}_{0.67}\text{Co}_{0.90}\text{Ti}_{0.10}\text{O}_2$ according to Na content.	48
Figure 2. 13 Transmission in situ XRD analysis of (a) $\text{Na}_{0.67}\text{CoO}_2$ and (b) $\text{Na}_{0.67}\text{Co}_{0.90}\text{Ti}_{0.10}\text{O}_2$ from 10 to 50° during the first charge. Peaks with asterisk are diffraction peaks of in situ cell parts.	49

Contents

Abstract	i
List of Tables	iv
List of Figures	v
Chapter 1. Introduction	1
1.1 Sodium ion batteries	1
1.1.1 General introduction	1
1.1.2 P2-type layered transition metal oxide positive electrode materials in sodium ion batteries.....	5
1.1.3 Three types of ordering in P2-type SIB layered transition metal oxide materials.....	13
1.2. Reference	15
Chapter 2. Na⁺/Vacancy Disordered P2-Na_{0.67}Co_{1-x}Ti_xO₂: High-Energy and High-Power Cathode Materials for Sodium Ion Batteries	17
2.1. Introduction.....	17
2.2. Results and discussion	20
2.3. Conclusions.....	51
2.4. Experimental section.....	52
2.4.1. Materials Synthesis.....	52
2.4.2. Structural Analysis.....	52
2.4.3. Electrochemical Method.....	53
2.4.4. Transmission in Situ XRD Analysis	53
2.4.5 Electrochemical characterization of materials.....	54
2.5. References.....	55

국 문 초 록.....59

Chapter 1. Introduction

1.1 Sodium ion batteries

1.1.1 General introduction

Since their successful commercialization in 1991, lithium ion batteries (LIBs), which consist of two lithium insertion electrodes to avoid lithium metal related safety issues, have become the most credible power sources for portable electronic devices (e.g. laptop and mobile phone) by virtue of their higher gravimetric and volumetric energy densities compared to other existing rechargeable batteries such as nickel-cadmium batteries and nickel-metal hydride batteries. [1-3] Moreover, as the demand for large-scale equipment such as electric vehicles (EVs) and energy storage systems (ESSs) has been increasing due to growing concern about global environmental issues such as global warming, LIBs now have been preferred power sources for large-scale applications because they satisfy the requirements as large-scale power sources including long cycle, high energy density, large output power, and high operating voltage. [4] However, uneven distribution of lithium resources in the Earth and rising cost of lithium, cobalt, and nickel resources are emerging as the primary concerns, which hinder the rapid development of the large-scale LIBs market. [5] Therefore, the alternatives to the LIBs have attracted enormous research effort in recent years.

Among the alternatives, sodium ion batteries (SIBs) are considered as attractive and promising alternatives especially for large-scale stationary applications such as ESSs because sodium resources are earth-abundant, evenly distributed across the world, and cost-effective compared to lithium resources and sodium is the second-lightest and -smallest alkali metal next to lithium. [6-8] Additionally, SIBs share the

same electrochemistry and basic principles with LIBs, which enable SIBs to exploit the-state-of-the art technology built up in LIBs. However, there are some obvious differences between two systems, which is originate from different charge carriers (Table 1.1). Na^+ ion (1.02 Å) is larger than Li^+ ion (0.76 Å), which contributes to the differences in phase stability, transport properties, and interphase formation. And, sodium (23 g mol^{-1}) is heavier than lithium (6.9 g mol^{-1}) and has a higher standard electrode potential (-2.71 V vs. SHE for Na and -3.02 V vs. SHE for Li), which lower gravimetric energy densities of SIBs compared to those of LIBs. However, the weight of electrode materials largely depends on the host structures that serve as electrodes, not on Li or Na. Thus, the theoretical difference in energy densities from mass of charge carriers is not significant (e.g. theoretical capacity is calculated to be 274 and 234 mAh g^{-1} for LiCoO_2 and NaCoO_2 , respectively). Also, sodium does not undergo alloy reaction with aluminum in SIBs operating voltage window, which enables SIBs to use aluminum as a cost-effective anode current collector instead of copper. [9]

A SIB cell is illustrated in Figure 1.1. A SIB cell consists of positive (cathode) and negative (anode) electrodes, which are able to insert or extract Na^+ ion inside them. And, the two electrodes are electronically separated by a separator and Na ion travels through electrolyte as a pure ionic conductor. The electrolyte consists of sodium containing salts and aprotic polar solvents. Unlike commercialized high-temperature Na/S and Na/ NiCl_2 batteries, SIBs operate at ambient temperature and exclude metallic sodium as the negative electrode. During charge process, Na^+ ions are extracted from the positive electrode, transferred via the electrolyte, and inserted to the negative electrode. Simultaneously, electrons are transferred from the positive

electrode to the negative electrode via external circuit. The reversal reaction occurs during the discharge process. The electrochemical performance of SIB including operating voltage, output power, and practical capacity is mainly determined by two electrode materials. Thus, for being a part of solution for future energy storage, great research effort has to be made in improving electrode materials for SIBs.

Table 1. 1 Comparison for Lithium and Sodium as charge carrier for rechargeable batteries. Adapted from Ref [6] (N. Yabuuchi, K. Kubota, M. Dahbi, S. Komaba, *Chem. Rev.*, **2014**, *114*, 11636).

	Li ⁺	Na ⁺
relative atomic mass	6.94	23.00
mass-to-electron ratio	6.94	23.00
Shannon's ionic radii/Å	0.76	1.02
E° (vs SHE)/V	-3.04	-2.71
melting point/°C	180.5	97.7
theoretical capacity of metal electrodes/mAh g ⁻¹	3861	1166
theoretical capacity of metal electrodes/mAh cm ⁻³	2062	1131
theoretical capacity of ACoO ₂ /mAh g ⁻¹	274	235
theoretical capacity of ACoO ₂ /mAh cm ⁻³	1378	1193
molar conductivity in ACIO ₄ /PC/S cm ² mol ⁻¹	6.54	7.16
desolvation energy in PC/kJ mol ⁻¹	218.0	157.3
coordination preference	octahedral and tetrahedral	octahedral and prismatic

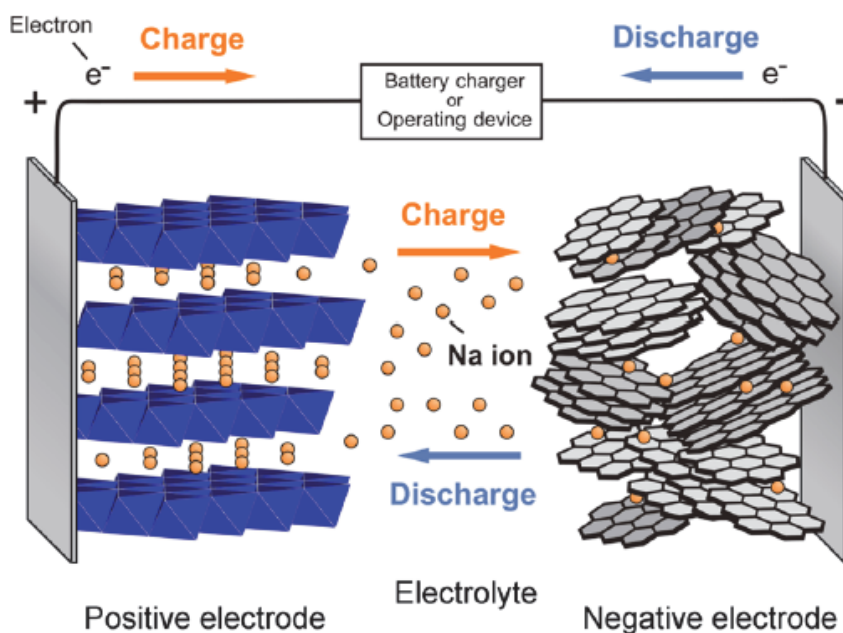


Figure 1. 1 Schematic illustration of the sodium ion batteries. Adapted from Ref [6] (N. Yabuuchi, K. Kubota, M. Dahbi, S. Komaba, *Chem. Rev.*, **2014**, *114*, 11636).

1.1.2 P2-type layered transition metal oxide positive electrode materials in sodium ion batteries

Positive electrode materials in SIBs are typically based on the Na-containing intercalation reaction, which insert/extract charge carriers (Na^+ in this context) into/from interstitial sites of a host material, for structural stability and reversible operating of SIBs. [6-8] Oxides, polyanions, and Prussian blue analogues are promising classes as SIB positive electrode materials as shown in Figure 1.2.

Among these classes, layered-type sodium-containing transition metal oxides (Na_xMO_2 , M = transition metal) have been the most extensively explored class due to their large energy densities and long cycle lives, similar to Li counterparts (Li_xMO_2) of LIBs. The crystal structures of layered Na_xMO_2 are shown in Figure 1.3. The structures of Na_xMO_2 consist of sheets of edge-sharing MO_6 octahedra stacked along the *c*-axis, where sodium ions are accommodated at octahedral and prismatic sites between MO_6 sheets. There are various polymorphs for the layered structure depending on stacking manners of MO_6 sheets. Delmas *et al.* proposed classification for the polymorphs. [10] In SIBs, O3-type and P2-type are two main groups of the layered compounds. O and P denote prismatic sites and octahedral sites of sodium, respectively, and the following numbers indicate the stacking manner of the close-packed oxygen layer (O3 = AB BC CA AB BC CA and P2 = AB BA AB BA). In terms of layered oxide material design, sodium ion offers more flexibility than lithium ion because its relatively larger ionic radius compared to those of 3d transition metals could prevent interlayer cationic mixing. For example, synthesis of cation-ordered $\text{LiNi}_{0.5}\text{Mn}_{0.5}\text{O}_2$ is very complicated while cation-ordered $\text{NaNi}_{0.5}\text{Mn}_{0.5}\text{O}_2$ can be easily synthesized. [11]

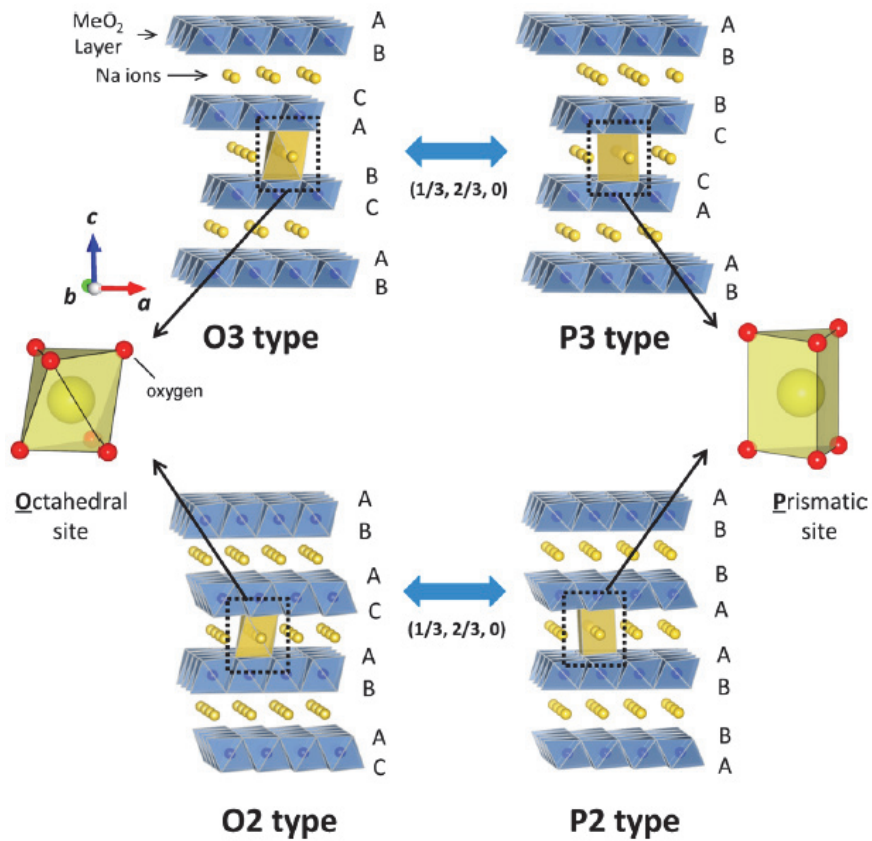


Figure 1. 3 Structures of SIB layered type transition metal oxide polymorphs. Adapted from Ref [6] (N. Yabuuchi, K. Kubota, M. Dahbi, S. Komaba, *Chem. Rev.*, **2014**, *114*, 11636).

Typically, the P2-type phase can be synthesized when a sodium deficiency is applied ($0.6 < x < 0.7$ in Na_xMO_2). The trigonal prismatic environment of Na site is distinct feature of SIB layered oxide from Li counterparts, which is energetically stabilized by large Na ion. The prismatic environment for Na is expected to offer more facile diffusion pathway than octahedral environment due to its open path for Na ion (Figure 1.4). P2-type $\text{Na}_{2/3}[\text{Ni}_{1/3}\text{Mn}_{2/3}]\text{O}_2$ and $\text{Na}_{2/3}[\text{Fe}_{1/2}\text{Mn}_{1/2}]\text{O}_2$ are representative examples in P2-type SIB layered oxide materials.

P2- $\text{Na}_{2/3}[\text{Ni}_{1/3}\text{Mn}_{2/3}]\text{O}_2$ reported by Lu *et al.* was proved to have a high operating voltage (~ 3.5 V vs. Na^+/Na) and a moderate specific capacity (~ 160 mAh g^{-1}) by utilizing $\text{Ni}^{2+/4+}$ redox. [12] Unlike other Na-containing layered oxides, P2- $\text{Na}_{2/3}[\text{Ni}_{1/3}\text{Mn}_{2/3}]\text{O}_2$ is well known to have air stability, which is expected from in-plane honeycomb ordering between Ni and Mn (NiMn_6). [13] When charged above 4.1 V vs. Na^+/Na where a considerable amount of Na ion is extracted, P2- $\text{Na}_{2/3}[\text{Ni}_{1/3}\text{Mn}_{2/3}]\text{O}_2$ undergoes a phase transition to the O2 phase. [14] This phase transition is accompanied by the gliding of MO_2 slabs and re-coordination of Na ions from prismatic sites to octahedral sites with drastic contraction of crystal structure along the *c*-axis. This P2-O2 phase transition at high voltage of P2- $\text{Na}_{2/3}[\text{Ni}_{1/3}\text{Mn}_{2/3}]\text{O}_2$ leads to the deterioration of electrode material with severe voltage and capacity decay. To overcome this issue, various solutions have been made by partially employing other metal ions (Mg^{2+} , Zn^{2+} , Cu^{2+} , ...) instead of Ni ions. [15] The metal substituted $\text{Na}_{2/3}[\text{Ni}_{1/3}\text{Mn}_{2/3}]\text{O}_2$ electrodes exhibit more stable cyclability than that of pristine electrode due to the mitigation of P2-O2 phase transition and Na^+ /vacancy ordering.

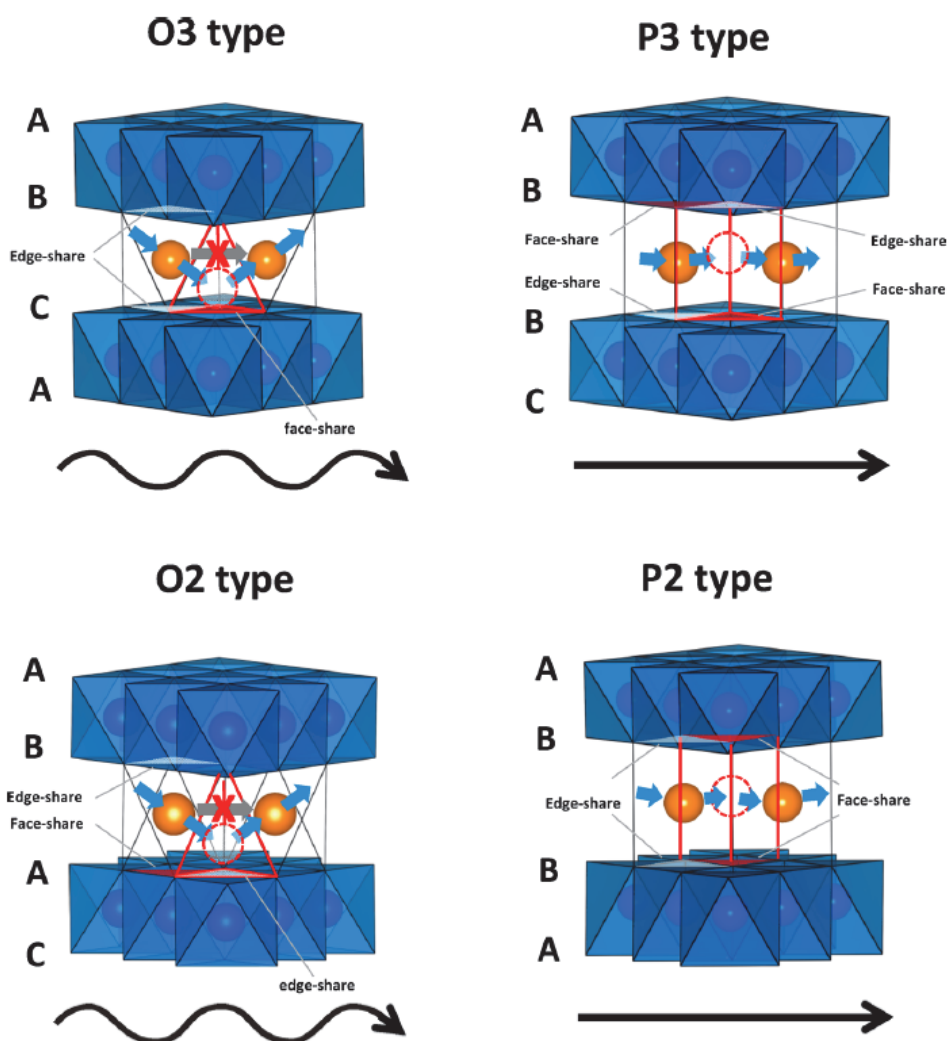


Figure 1. 4 Na diffusion pathway in different SIB layered polymorphs. Adapted from Ref [6] (N. Yabuuchi, K. Kubota, M. Dahbi, S. Komaba, *Chem. Rev.*, **2014**, *114*, 11636).

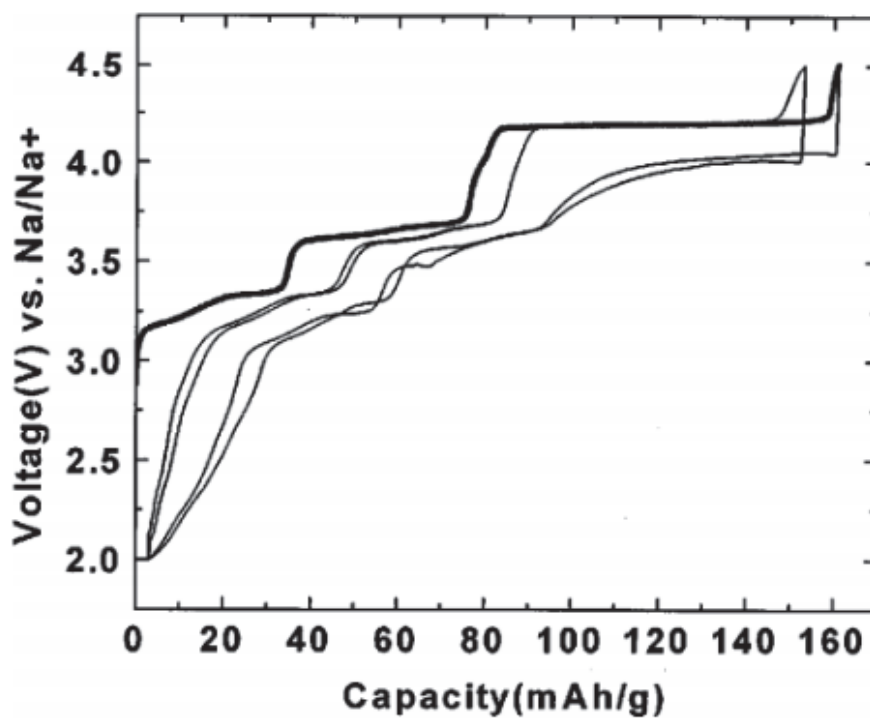


Figure 1. 5 Voltage-capacity profile for a Na/P2-Na_{2/3}[Ni_{1/3}Mn_{2/3}]O₂ cell. Adapted from Ref [12] (Z. Lu, J. R. Dahn, *J. Electrochem. Soc.*, **2001**, 148, A1225).

P2-Na_{2/3}[Fe_{1/2}Mn_{1/2}]O₂, which was reported by Yabuuchi et al., is another promising P2-type layered positive electrode materials due to its Earth-abundant elements. [16] It exhibits a large reversible discharge capacity of 190 mAh g⁻¹ by introducing Fe^{3+/4+} redox reaction at high voltage, which is inactive in LiFeO₂ of LIBs. Unlike to the abovementioned P2-Na_{2/3}[Ni_{1/3}Mn_{2/3}]O₂, P2-Na_{2/3}[Fe_{1/2}Mn_{1/2}]O₂ undergoes a different phase transition at high voltage from P2 phase to “OP4” or “Z” phase, which leads to less severe volume change than P2-O2 transition. [17] The new evolved phase has poor crystallinity especially along the *c*-axis rather than *a*- and *b*-axis, which is formed along with transition metal migration into Na layer. This migration is reversible, although it leads to polarization. Addition of other metal (e.g. Ni) instead of Fe was prove to mitigate the Fe migration improving to cyclability. Recently, Somerville et al. described the accurate structure of “Z” phase as a continuously changing intergrowth structure which evolves between P2 and O2 with OP4 as an intermediary. [18]

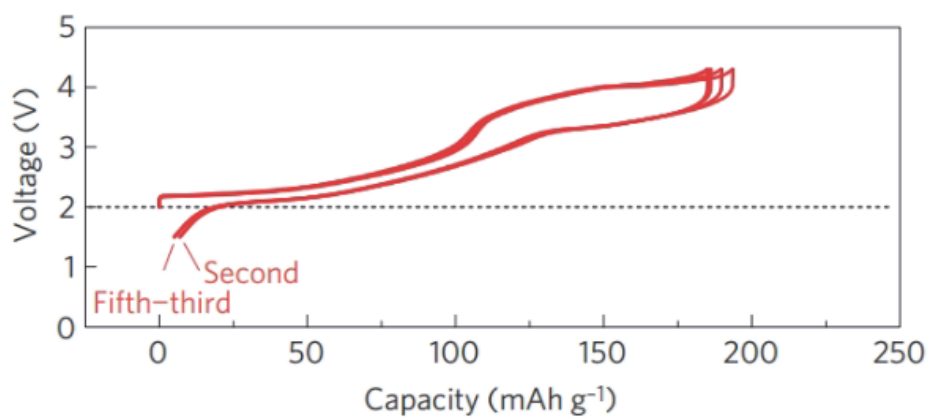


Figure 1. 6 Voltage-capacity profile for a Na/P2-Na_{2/3}[Fe_{1/2}Mn_{1/2}]O₂ cell. Adapted from Ref [16] (N. Yabuuchi, M. Kajiyama, J. Iwatate, H. Nishikawa, S. Hitomi, R. Okuyama, R. Usui, Y. Yamada, S. Komaba, *Nat. Mater.*, **2012**, *11*, 512).

1.1.3 Three types of ordering in P2-type SIB layered transition metal oxide materials

There are three different types of ordering in P2-type layered transition metal oxide materials. [19] The first one is cation ordering (M_1/M_2 ordering) in transition metal layer, which is mainly controlled by difference in ionic radii between M_1 and M_2 ions and their atomic ratio. Cation ordering is favorable when the radii difference is higher than 15%; otherwise cation disordering is favorable. The other two are coupled to each other: charge ordering and Na^+ /vacancy ordering. The charge ordering is controlled by the difference in redox potentials between the M_1 and M_2 ions. When the difference in redox potential is small, charge ordering is favored and *vice versa*. The last one is Na^+ /vacancy ordering that is in-plane patterning between Na^+ and vacancy sites in Na layer, which is coupled to the charge ordering. It is caused by an energy minimization between electrostatic interactions of metal ions below a critical temperature. [20] Also, it is very sensitive to Na content in the host, and thus, the first-order transition with a voltage step occurs when Na content is controlled at a particular point. These transitions of layered transition metal oxides act as kinetic barriers in battery application, leading to lower considerably Na^+ diffusivity. [21] Na_xCoO_2 and Na_xVO_2 are representative examples, which exhibit the complicated charge/discharge behavior due to their Na^+ /vacancy orderings. [22,23] Thus, many research efforts have been made to mitigate the Na^+ /vacancy ordering to realize high-power SIB positive electrode materials. [19,24,25]

Table 1. 2 Disordered/Ordered structure in P2-type layered transition metal oxides $\text{Na}_x[\text{M}_1\text{M}_2]\text{O}_2$. Adapted from Ref [19] (Y. Wang, R. Xiao, Y.-S. Hu, M. Avdeev, L. Chen, *Nat. Commun.*, **2015**, 6, 6954).

No.	Formula	Ratio of ionic radii	M_1/M_2 ordering	Charge ordering	$\text{Na}^+/\text{vacancy}^*$
1	$\text{Na}_{0.74}\text{CoO}_2$	1.15		ordered	ordered
2	Na_xVO_2	1.10		ordered	ordered
3	$\text{Na}_{0.6}\text{MnO}_2$	1.22		ordered	ordered
4	$\text{Na}_{5/8}\text{MnO}_2$	1.22		ordered	ordered
5	$\text{Na}_{0.7}\text{MnO}_2$	1.22		ordered	ordered
6	$\text{Na}_{2/3}[\text{Co}_{2/3}\text{Mn}_{1/3}]\text{O}_2$	1.15	disordered	ordered	ordered
7	$\text{Na}_{0.79}[\text{Co}_{0.7}\text{Mn}_{0.3}]\text{O}_2$	1.15	disordered	ordered	ordered
8	$\text{Na}_{2/3}[\text{Co}_{1/3}\text{Mn}_{2/3}]\text{O}_2$	1.15	disordered	disordered	disordered
9	$\text{Na}_{2/3}[\text{Ni}_{1/3}\text{Mn}_{2/3}]\text{O}_2$	1.30	ordered	ordered	ordered
10	$\text{Na}_{2/3}[\text{Ni}_{1/3}\text{Mn}_{2/3-x}\text{Ti}_x]\text{O}_2$ ($x < 1/6$) [#]	1.30	ordered	ordered	ordered
10	$\text{Na}_{2/3}[\text{Ni}_{1/3}\text{Mn}_{2/3-x}\text{Ti}_x]\text{O}_2$ ($x \geq 1/6$) [#]	1.14	disordered	disordered	disordered
12	$\text{Na}_{0.7}[\text{Ni}_{0.3}\text{Co}_{0.1}\text{Mn}_{0.6}]\text{O}_2$ [#]	1.30	ordered	ordered	ordered
13	$\text{Na}_{0.67}[\text{Ni}_{0.15}\text{Co}_{0.2}\text{Mn}_{0.65}]\text{O}_2$ [#]	1.13	disordered	disordered	disordered
14	$\text{Na}_{0.67}[\text{Ni}_{0.15}\text{Fe}_{0.2}\text{Mn}_{0.65}]\text{O}_2$ [#]	1.07	disordered	disordered	disordered
15	$\text{Na}_{2/3}[\text{Ni}_{1/3}\text{Ti}_{2/3}]\text{O}_2$	1.14	disordered	disordered	disordered
16	$\text{Na}_{2/3}[\text{Fe}_{1/3}\text{Mn}_{2/3}]\text{O}_2$	1	disordered	disordered	disordered
17	$\text{Na}_{2/3}[\text{Fe}_{1/2}\text{Mn}_{1/2}]\text{O}_2$	1	disordered	disordered	disordered
18	$\text{Na}_{2/3}[\text{Co}_{1/3}\text{Ti}_{2/3}]\text{O}_2$	1.07	disordered	disordered	disordered
19	$\text{Na}_{0.67}[\text{Mg}_{0.28}\text{Mn}_{0.72}]\text{O}_2$	1.12	disordered	disordered	disordered
20	$\text{Na}_{0.85}[\text{Li}_{0.17}\text{Ni}_{0.21}\text{Mn}_{0.64}]\text{O}_2$	1.02	disordered	disordered	disordered
21	$\text{Na}_{0.66}[\text{Li}_{0.22}\text{Ti}_{0.78}]\text{O}_2$	1.26	disordered	disordered	disordered
22	$\text{Na}_{0.6}[\text{Cr}_{0.6}\text{Ti}_{0.4}]\text{O}_2$	1.02	disordered	disordered	disordered
23	$\text{Na}_2\text{Ni}_2\text{TeO}_6$ ($\text{Na}_{2/3}[\text{Ni}_{2/3}\text{Te}_{1/3}]\text{O}_2$)	1.23	ordered	disordered	disordered

1.2. Reference

- [1] M. Armand, J.-M. Tarascon, *Nature*, **2008**, *451*, 652.
- [2] J.-M. Tarascon, M. Armand, *Nature*, **2001**, *414*, 359.
- [3] M. Li, J. Lu, Z. Chen, K. Amine, *Adv. Mater.*, **2018**, *30*, 1800561.
- [4] B. Dunn, H. Kamath, J.-M. Tarascon, *Science*, **2011**, *334*, 928.
- [5] J.-M. Tarascon, *Nat. Chem.*, **2010**, *2*, 510.
- [6] N. Yabuuchi, K. Kubota, M. Dahbi, S. Komaba, *Chem. Rev.*, **2014**, *114*, 11636.
- [7] J.-Y. Hwang, S.-T. Myung, Y.-K. Sun, *Chem. Soc. Rev.*, **2017**, *46*, 3529.
- [8] X. Pu, H. Wang, D. Zhao, H. Yang, X. Ai, S. Cao, Z. Chen, Y. Cao, *Small*, **2019**, *15*, 1805427.
- [9] C. Vaalma, D. Buchholz, M. Weil, S. Passerini, *Nat. Rev. Mater.*, **2018**, *3*, 18013.
- [10] C. Delmas, C. Fouassier, P. Hagenmuller, *Physica B+C*, **1980**, *99*, 81.
- [11] K. Kang, Y. S. Meng, J. Bréger, C. P. Grey, G. Ceder, *Science*, **2006**, *311*, 977.
- [12] Z. Lu, J. R. Dahn, *J. Electrochem. Soc.*, **2001**, *148*, A1225.
- [13] K. Hemalatha, M. Jayakumar, P. Bera and A. S. Prakash, *J. Mater. Chem. A*, **2015**, *3*, 20908.
- [14] D. H. Lee, J. Xu, Y. S. Meng, *Phys. Chem. Chem. Phys.*, **2013**, *15*, 3304.
- [15] J. Zhang, W. Wang, W. Wang, S. Wang, B. Li, *ACS Appl. Mater. Interfaces*, **2019**, *11*, 22051.
- [16] N. Yabuuchi, M. Kajiyama, J. Iwatate, H. Nishikawa, S. Hitomi, R. Okuyama, R. Usui, Y. Yamada, S. Komaba, *Nat. Mater.*, **2012**, *11*, 512.
- [17] E. Talaie, V. Duffort, H. L. Smith, B. Fultz, L. F. Nazar, *Energy Environ. Sci.*, **2015**, *8*, 2512.

- [18] J. W. Somerville, A. Sobkowiak, N. Tapia-Ruiz, J. Billaud, J. G. Lozano, B. A. House, L. C. Gallington, T. Ericsson, L. Häggström, M. R. Roberts, U. Maitra, P. G. Bruce, *Energy Environ. Sci.*, **2019**, *12*, 2223.
- [19] Y. Wang, R. Xiao, Y.-S. Hu, M. Avdeev, L. Chen, *Nat. Commun.*, **2015**, *6*, 6954.
- [20] M. Roger, D. J. Morris, D. A. Tennant, M. J. Gutmann, J. P. Goff, J. U. Hoffmann, R. Feyerherm, E. Dudzik, D. Prabhakaran, A. T. Boothroyd, N. Shannon, B. Lake, P. P. Deen, *Nature*, **2007**, *445*, 631.
- [21] A. J. Toumar, S. P. Ong, W. D. Richards, S. Dacek, G. Ceder, *Phys. Rev. Appl.*, **2015**, *4*, 064002.
- [22] R. Berthelot, D. Carlier, C. Delmas, *Nat. Mater.*, **2011**, *10*, 74.
- [23] M. Guignard, C. Didier, J. Darriet, P. Bordet, E. Elkaim, C. Delmas, *Nat. Mater.*, **2013**, *12*, 74.
- [24] P.-F. Wang, H.-R. Yao, X.-Y. Liu, Y.-X. Yin, J.-N. Zhang, Y. Wen, X. Yu, L. Gu, Y.-G. Guo, *Sci. Adv.*, **2018**, *4*, eaar6018.
- [25] N. Bucher, S. Hartung, J. B. Franklin, A. M. Wise, L. Y. Lim, H.-Y. Chen, J. N. Weker, M. F. Toney, M. Srinivasan, *Chem. Mater.*, **2016**, *28*, 2041.

Chapter 2. Na⁺/Vacancy Disordered P2-Na_{0.67}Co_{1-x}Ti_xO₂: High-Energy and High-Power Cathode Materials for Sodium Ion Batteries

*The work presented in Chapter 2 was published in *ACS Appl. Mater. Interfaces*, **2018**, 10, 3562.

2.1. Introduction

Lithium ion batteries (LIBs) are considered one of the most credible energy conversion and storage systems for small portable devices, including laptops and mobile phones. [1,2] Owing to global warming and the negative perception of nuclear power generation, electric vehicles (EVs) and energy storage systems (ESSs) have emerged as potential environmentally friendly options and have expanded the field of application of rechargeable batteries from small devices to large-scale equipment. However, large facilities require large power sources capable of handling hundreds of kWh or MWh of energy. Many researchers have pointed out that the limited availability of lithium ion resources can inhibit the market of LIBs from expanding to industries involving large equipment. [3] On the other hand, sodium resources are abundant and inexpensive compared to lithium resources. Thus, the problem of high cost can be potentially solved by simply replacing lithium ions with sodium ions for the successful development of EVs and ESSs. With this background, sodium ion batteries (SIBs) have attracted much attention as an affordable alternative to LIBs in the near future. [4-8]

As large devices of EVs and ESSs require huge batteries, it is very important to increase the energy capacity to reduce the space required for the battery and the cost of production. However, sodium has larger ionic radii, atomic weight, and a more positive redox potential than lithium. Therefore, SIBs have lower gravimetric and volumetric energy densities than LIBs. As such, an effective strategy for developing SIBs with high energy densities is essential for successfully replacing LIBs. Among positive electrode materials for SIBs, layer structured Na_xMO_2 (M = Mn, Fe, Co, Ni, etc.) compounds are promising because of their large energy densities and long cycle lives. [9-15] Similar to the cathode of LIBs, the layer structure of these materials consists of edge-sharing MO_6 octahedra stacking along the *c*-axis and Na ions intercalated between the MO_2 layers. Various polymorphs are possible for a layered Na_xMO_2 compound depending on the crystal structure. According to the classification proposed by Delmas *et al.*, P2-type and O3-type layered structures are the most common in SIBs. [16] P and O denote sodium ions in the prismatic and octahedral sites, respectively, and the corresponding numbers are the stacking manner of the close-packed oxygen layer (for instance, AB BA AB BA and AB BC CA AB BC CA, respectively). Na_xCoO_2 is the first reported layered oxide to be used as an Na intercalation host for the cathode of SIBs. [17] Unlike LiCoO_2 , the P2-type Na_xCoO_2 (NCO) exhibits a very complicated electrochemical charge/discharge curve with several voltage plateaus. [18] These plateaus are caused by Na^+ /vacancy ordering that is present in in-plane patterning between Na^+ and vacancy sites and absent in the layer structure cathode for LIBs. Na^+ /vacancy ordering is a result of energy minimization among three possible cation interactions of Na^+-Na^+ , $\text{Na}^+-\text{Co}^{3+/4+}$, and $\text{Co}^{3+/4+}-\text{Co}^{3+/4+}$ below a critical temperature. [19] It is very sensitive to

Na content in the host, and thus, Na⁺/vacancy ordering is accompanied by the first-order transition at a particular Na content. [20] This type of ordering can also be seen in various other layered oxides. [21-24] This transition naturally causes an additional activation energy barrier for Na⁺ accommodations. [25] Furthermore, similar to LiCoO₂ in LIBs, the large desodiation from the octahedral sites surrounded by oxygen ions also causes irreversible changes in the crystal structure owing to the unstable state of oxygen ions directly facing each other without sodium ions. [26,27] Thus, the electrochemical extraction of Na ions should be limited to the range where the crystal structure of cathodes is not altered, and therefore, the practical capacity of the P2-type is much lower than the theoretical capacity (235 mAh g⁻¹), which is calculated based on maximum Na ion utilization of NaCoO₂. Considering the aforementioned factors, a large amount of Na ion utilization during cycling is significantly beneficial to the improvement of the energy density of SIBs.

Many studies have focused on improving diffusivity and rate capability by controlling Na⁺/vacancy ordering through doping or substitution. Wang *et al.* reported that Na⁺/vacancy disordered materials can be designed by simultaneously mitigating charge and cation ordering through the selection of appropriate doping of transition metals. [28] This could provide excellent rate capability and cyclability. There have been several reports on the relationship between the relaxation of ordering and the increase in rate capability. [29-31] In this study, we investigated positive solutions of improving energy density and electrochemical stability by controlling Na⁺/vacancy disordering. For the P2-type NCO, we synthesized various P2-type Na_{0.67}Co_{1-x}Ti_xO₂ ($x = 0, 0.05, 0.1, 0.15, \text{ and } 0.2$) by partial substitution of Ti ions on Co ions of NCO to control the Na⁺/vacancy ordering. Previously, Sabi *et al.*

reported the sodiation/desodiation mechanism of P2- $\text{Na}_{2/3}\text{Co}_{0.95}\text{Ti}_{0.05}\text{O}_2$ in the potential window 2–4.2 V. [32] In this paper, we report highly improved electrochemical properties of $\text{Na}_{0.67}\text{Co}_{0.9}\text{Ti}_{0.1}\text{O}_2$ at particularly high voltages compared to Na^+ /vacancy ordered NCO. We also report a mechanism for irreversible reactions of highly desodiated NCO accompanied by a severe capacity decay using selected area electron diffraction (SAED) analysis. Furthermore, differences in structural evolution caused by disordering were investigated through in situ X-ray diffraction (in situ XRD) analysis.

2.2. Results and discussion

The structure of the P2-type layered $\text{Na}_{0.67}\text{Co}_{1-x}\text{Ti}_x\text{O}_2$ is illustrated in Figure 2.1a. Na ions occupy prismatic sites, which are categorized into two types: Na1 (face shared with CoO_6 octahedra, yellow sphere) and Na2 (edge shared with CoO_6 octahedra, pink sphere). The surface morphologies of the prepared powder samples are shown in Figure 2.2. All samples have a similar morphology with irregular particle sizes. Figure 2.2b shows synchrotron X-ray powder diffraction (SXRPD) patterns of as-prepared powder samples. The prepared $\text{Na}_{0.67}\text{CoO}_2$ exhibited the P2-type SXRPD pattern of the space group of $\text{P6}_3/\text{mmc}$ in Figure 2.1a. Similarly, samples with Ti substitution up to $x = 0.1$ in the form of $\text{Na}_{0.67}\text{Co}_{1-x}\text{Ti}_x\text{O}_2$ did not contain any other new peaks, except for the peaks of a phase where the P2-type layered structure was the same as that of P2-type NCO. The SXRPD patterns of samples with $\text{Na}_{0.67}\text{Co}_{0.85}\text{Ti}_{0.15}\text{O}_2$ and $\text{Na}_{0.67}\text{Co}_{0.8}\text{Ti}_{0.2}\text{O}_2$ have new peaks at 15.41, 31.08, 35.62, 40.47, 43.77, 51.21, and 55.52° of 2θ (asterisks in Figure 2.1b), which can be clearly separated from the major phase of the space group of $\text{P6}_3/\text{mmc}$. Additionally, as the substituted amount of Ti ions increases from 0.15 to 0.2, the new peaks become

stronger and more prominent (as shown in the inset of Figure 2.1b). A small amount of Ti (below $x = 0.1$) can be successfully doped in the P2-type structure without changes in the crystal structure, but a large amount of Ti substitution (above $x = 0.15$) causes the formation of the unfavorable second-phases. Therefore, we limited the amount of Ti substitution to less than 0.1 in order to avoid the negative effects of the second-phase.

Figure 2.1c shows changes in the lattice parameter of a and unit cell volume V with various amounts of Ti. Based on the presence of Ti^{4+} , the parameters are obtained by using the Rietveld refinement. Further details are provided in Tables 2.1 and 2.2. The lattice parameter a increases when the amount of Ti^{4+} increases from 0 to 0.1, expanding unit cell volume. Because the ionic radius of Ti^{4+} (60.5 pm) is larger than that of Co^{4+} (53 pm), it is believed that Ti substitution causes expansion of the MO_2 slab and Ti ions of TiO_2 are successfully doped in $\text{Na}_{0.67}\text{Co}_{1-x}\text{Ti}_x\text{O}_2$ during our designed material synthesis process. In the enlarged SXRPD pattern of P2-type NCO between 26.0° to 32.5° shown in Figure 2.1d, three superstructure peaks are observed. These peaks originates from the in-plane Na^+ /vacancy ordering. [33] However, Ti substitution gradually decreases the intensities of these peaks depending on the amount of substituted Ti indicating that Ti substitution effectively mitigates the Na^+ /vacancy ordering in P2-type NCO. As a result, no superstructure peak is observed in $\text{Na}_{0.67}\text{Co}_{0.90}\text{Ti}_{0.10}\text{O}_2$. The atomic compositions were confirmed by ICP-AES analysis for single-phase samples ($x = 0, 0.05, \text{ and } 0.1$) as shown in Table 2.3. Measured ratios of the samples matched well with the designed values.

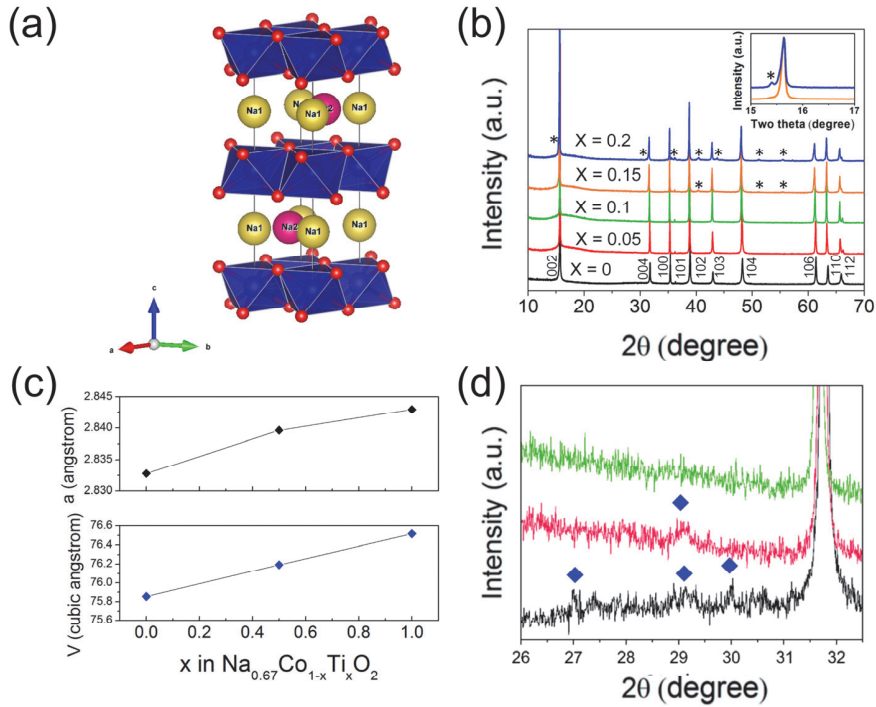


Figure 2. 1 (a) Schematic illustration of the P2-type $\text{Na}_{0.67}\text{Co}_{1-x}\text{Ti}_x\text{O}_2$ crystal structure. Two different sites exist for Na; Na1 and Na2. (b) Synchrotron X-ray powder diffraction (SXRPD) patterns of $\text{Na}_{0.67}\text{Co}_{1-x}\text{Ti}_x\text{O}_2$ ($x = 0, 0.05, 0.1, 0.15,$ and 0.2). The wavelength of the radiation is 1.49150 \AA . Inset shows a peak from an unknown impurity phase near the (002) peak. The asterisks indicate impurity phases. (c) Variations of lattice parameter of a and unit cell volume V with the amount of substituted Ti^{4+} in $\text{Na}_{0.67}\text{Co}_{1-x}\text{Ti}_x\text{O}_2$ ($x = 0, 0.05,$ and 0.1) (d) Enlarged SXRPD patterns of $\text{Na}_{0.67}\text{Co}_{1-x}\text{Ti}_x\text{O}_2$ ($x = 0, 0.05,$ and 0.1) between 26.0° to 32.5° . The blue diamonds indicate superstructure peaks from Na^+ /vacancy ordering.

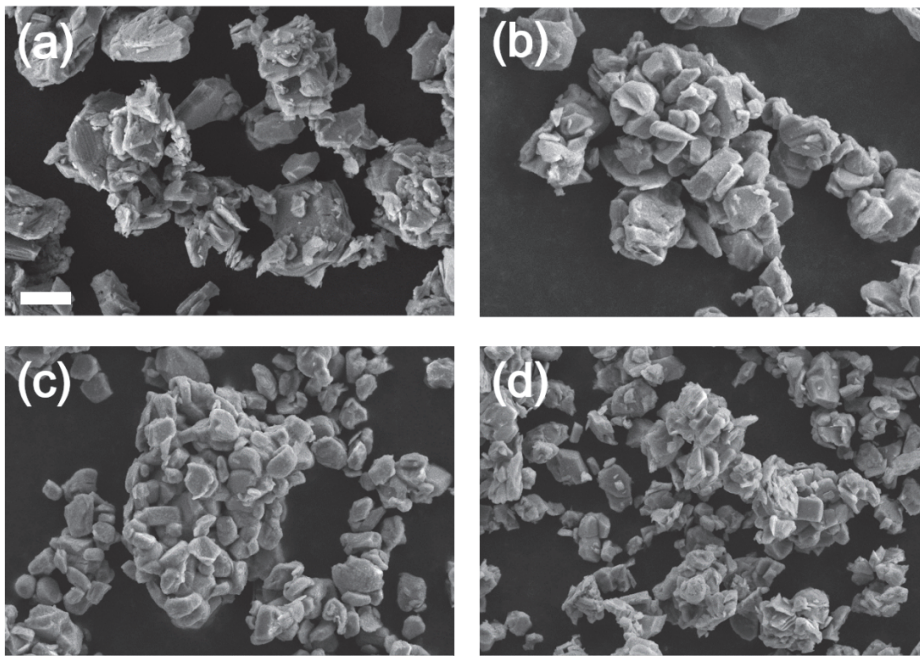


Figure 2. 2 FE-SEM images of as-synthesized P2-type (a) $\text{Na}_{0.67}\text{CoO}_2$, (b) $\text{Na}_{0.67}\text{Co}_{0.95}\text{Ti}_{0.05}\text{O}_2$, (c) $\text{Na}_{0.67}\text{Co}_{0.90}\text{Ti}_{0.10}\text{O}_2$, and (d) $\text{Na}_{0.67}\text{Co}_{0.85}\text{Ti}_{0.15}\text{O}_2$ powder samples. Scale bar = 5 μm .

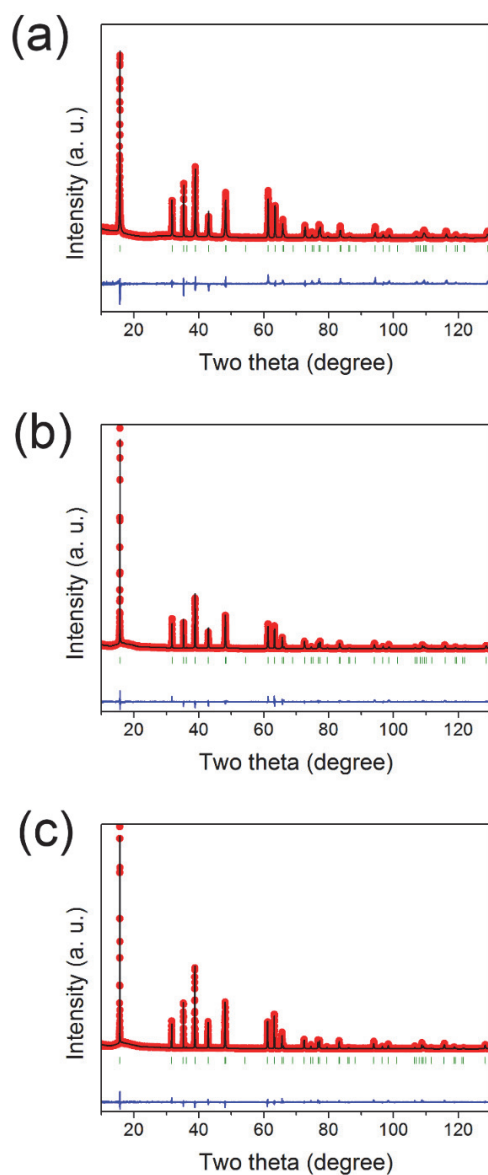


Figure 2. 3 Rietveld plots for P2-type (a) $\text{Na}_{0.67}\text{CoO}_2$, (b) $\text{Na}_{0.67}\text{Co}_{0.95}\text{Ti}_{0.05}\text{O}_2$, and (c) $\text{Na}_{0.67}\text{Co}_{0.90}\text{Ti}_{0.10}\text{O}_2$ obtained by refining SXRPD data. The red dots and black solid lines indicate the observed and calculated patterns, respectively. The blue solid lines indicate their difference, and the green tick marks indicate the peak positions of the diffraction.

Table 2. 1 Unit cell constants and atomic parameters of P2-type (a) $\text{Na}_{0.67}\text{CoO}_2$, (b) $\text{Na}_{0.67}\text{Co}_{0.95}\text{Ti}_{0.05}\text{O}_2$, and (c) $\text{Na}_{0.67}\text{Co}_{0.90}\text{Ti}_{0.10}\text{O}_2$ samples calculated from Rietveld refinement of SXRD data.

Table 2. 1 a						
Theoretical formula	$\text{Na}_{0.67}\text{CoO}_2$					
ICP-AES result	$\text{Na}_{0.66}\text{CoO}_2$					
space group	P6 ₃ /mmc (No. 194)					
a = b = 2.83277(2) Å, c = 10.9150(1) Å, V = 75.854(1) Å ³						
alpha = 90 °, beta = 90 °, gamma = 120 °						
R _{wp} = 12.8 %, R _p = 10.0 %, GOF = 1.67						
Atom	site	x	y	z	Occupancy	<i>U</i> _{iso} (Å ²)
Na1(Na _f)	2 <i>b</i>	0	0	1/4	0.23(2)	0.035(11)
Na2(Na _e)	2 <i>c</i>	2/3	1/3	3/4	0.43(2)	0.011(2)
Co	2 <i>a</i>	0	0	0	1 ^a	0.00127 ^a
O	4 <i>f</i>	2/3	1/3	0.0809(2)	1 ^a	0.012(2)

^aFixed parameter

Table 2. 1 b						
Theoretical formula	$\text{Na}_{0.67}\text{Co}_{0.95}\text{Ti}_{0.05}\text{O}_2$					
ICP-AES result	$\text{Na}_{0.66}\text{Co}_{0.95}\text{Ti}_{0.05}\text{O}_2$					
space group	P6 ₃ /mmc (No. 194)					
a = b = 2.83961(1) Å, c = 10.9113(1) Å, V = 76.194(1) Å ³						
alpha = 90 °, beta = 90 °, gamma = 120 °						
R _{wp} = 11.0 %, R _p = 8.07 % GOF = 1.58						
Atom	Site	x	Y	z	Occupancy	<i>U</i> _{iso} (Å ²)
Na1 (Na _f)	2 <i>b</i>	0	0	1/4	0.25(4)	0.088(7)
Na2 (Na _e)	2 <i>c</i>	2/3	1/3	3/4	0.43(2)	0.0024(2)
Co	2 <i>a</i>	0	0	0	0.95 ^a	0.00024 ^a
O	4 <i>f</i>	2/3	1/3	0.0821(2)	0.97(3)	0.0126(11)
Ti	2 <i>a</i>	0	0	0	0.05 ^a	0.00024 ^a

^aFixed parameter

Table 2. 1 c						
Theoretical formula	Na _{0.67} Co _{0.90} Ti _{0.10} O ₂					
ICP-AES result	Na _{0.66} Co _{0.90} Ti _{0.10} O ₂					
space group	P6 ₃ /mmc (No. 194)					
a = b = 2.84293(1) Å, c = 10.9319(1) Å, V = 76.517(1) Å ³						
alpha = 90 °, beta = 90 °, gamma = 120 °						
R _{wp} = 9.50 % R _p = 7.10 % GOF = 1.40						
Atom	site	x	y	z	Occupancy	U _{iso} (Å ²)
Na1(Na _f)	2b	0	0	1/4	0.25(2)	0.038(4)
Na2 (Na _e)	2c	2/3	1/3	3/4	0.43(2)	0.022(2)
Co	2a	0	0	0	0.90 ^a	0.00127 ^a
O	4f	1/3	2/3	0.0884(2)	1.00(2)	0.0018(7)
Ti	2a	0	0	0	0.10 ^a	0.00127 ^a

^aFixed parameter

Table 2. 2 Selected bond distances, MO₂ slab thickness, and NaO₂ interslab distance of P2-type Na_{0.67}CoO₂, Na_{0.67}Co_{0.95}Ti_{0.05}O₂, and Na_{0.67}Co_{0.90}Ti_{0.10}O₂ samples calculated from Rietveld refinement of SXRD data.

Selected bond distances			
(Å)			
	Na _{0.67} CoO ₂	Na _{0.67} Co _{0.95} Ti _{0.05} O ₂	Na _{0.67} Co _{0.90} Ti _{0.10} O ₂
M–O	1.859(1)	1.868(1)	1.905(1)
Na–O	2.466(2)	2.459(2)	2.411(2)
M–M	2.833(1)	2.840(1)	2.843(1)
MO ₂ slab thickness	1.766	1.792	1.933
NaO ₂ interslab distance	3.691	3.664	3.533

Table 2. 3 Atomic compositions of $\text{Na}_{0.67}\text{Co}_{1-x}\text{Ti}_x\text{O}_2$ ($x = 0, 0.05$ and 0.1) samples confirmed by ICP-AES analysis.

<i>Sample</i>	<i>Theoretical formula</i>	<i>Measured atomic ratio</i>
$x = 0$	$\text{Na}_{0.67}\text{CoO}_2$	$\text{Na}_{0.66}\text{CoO}_2$
$x = 0.05$	$\text{Na}_{0.67}\text{Co}_{0.95}\text{Ti}_{0.05}\text{O}_2$	$\text{Na}_{0.66}\text{Co}_{0.95}\text{Ti}_{0.05}\text{O}_2$
$x = 0.1$	$\text{Na}_{0.67}\text{Co}_{0.90}\text{Ti}_{0.10}\text{O}_2$	$\text{Na}_{0.66}\text{Co}_{0.90}\text{Ti}_{0.10}\text{O}_2$

To elucidate the effect of Ti substitution on the electrochemical properties of the P2-type NCO, each sample of $\text{Na}_{0.67}\text{Co}_{1-x}\text{Ti}_x\text{O}_2$ ($x = 0, 0.05, \text{ and } 0.1$) was tested at a constant current density of 100 mA g^{-1} between 2.0 and 4.4 V, which is much higher than the value used in previous studies. [34–37] In many previous papers, the cutoff potential for the P2-type NCO was controlled under 4 V to avoid the large amount of desodiation, because the possible irreversible changes in the crystal structure over 4.0 V can restrict long cycle life. [34–37] However, we set a high cutoff potential of 4.4 V to utilize a large number of sodium ions for high energy density. Figure 2.4a-c presents the charge/discharge voltage curves of each sample at the 1st, 2nd, 5th, 10th, 50th, and 100th cycles. Considering that the initial charge specific capacities of all cells are around 120 mAh g^{-1} , the stoichiometry of Na ions in the fully charged state is around 0.15. Similarly, all the discharge specific capacities reach about 140 mAh g^{-1} , implying that approximately 0.60 mol of Na^+ in a unit cell is reversibly accommodated.

The initial potentials of the first charging sequence in all cells were found to be lower than 2.75 V. Considering that the equilibrium potential of $\text{Ti}^{3+}/\text{Ti}^{4+}$ in the P2-type structure is about 0.8 V vs Na/Na^+ , it is very reasonable that the substituted Ti ions are mainly Ti^{4+} rather than Ti^{3+} , as described in Figure 2.1c. [38] In detail, the voltage curves of the P2-type NCO show very complicated voltage steps, having multiple plateaus as reported in the previous papers.¹⁸ For instance, the first charge curve has eight voltage plateaus at 2.70, 2.98, 3.17, 3.28, 3.67, 3.98, 4.19, and 4.37 V vs Na/Na^+ , as shown in the blue curve in Figure 2.4a. This is attributed to the Na^+ /vacancy ordering via first-order transitions at points having particular concentrations of vacancies and Na^+ . Focusing on the reversible behavior in the

initial discharge curve over 4.1 V, only one shortened discharging voltage plateau of 10 mAh g⁻¹ is observed at 4.25 V instead of two reversible plateaus being paired with two charging plateaus, which are shown in the initial charging curve having a capacity of 26.8 mAh g⁻¹. As expected, this sodiation/desodiation behavior in this high-potential range beyond 4.1 V is not completely reversible. Furthermore, this partially reversible voltage plateau over 4.2 V of the NCO is observed only in the first cycle and almost disappears in the second cycle. Thus, this capacity can be considered irreversible from the viewpoint of practical applications. The discharge capacity decreased from 146.0 mAh g⁻¹ at the first cycle to 133.2 mAh g⁻¹ at the second cycle. Meanwhile, other voltage steps at 2.28, 2.40, and 2.50 V were strictly maintained during the subsequent cycles. Therefore, plateaus relevant to Na⁺/vacancy ordering less than 4.1 V are well preserved during cycling unlike the abovementioned plateau over 4.1 V.

Subsequently, Ti is substituted in the NCO, and notable differences are found in the voltage curves of the cells with Ti substituted samples (Figure 2.4b and c). For Na_{0.67}Co_{0.95}Ti_{0.05}O₂, under 4 V, the plateaus of NCO become sloping lines rather than flat curves (Figure 2.4b). The plateaus in this region (Figure 2.4a) decrease or disappear. Similarly, when Ti is further substituted ($x = 0.1$, Na_{0.67}Co_{0.90}Ti_{0.10}O₂), all voltage plateaus disappear, except for a wide voltage drop at 3.5 V, as shown in Figure 2.4c. These results show that Ti substitution is effective for inducing desodiation of different modes, detouring Na⁺/vacancy ordering of the P2-type NCO. It is noteworthy that the voltage plateau of Na_{0.67}Co_{0.90}Ti_{0.10}O₂ at high potential beyond 4.1 V—related to the irreversible loss of NCO—does not appear. Over 4.1 V, the voltage curve becomes an inclined slope instead of a flat profile. Interestingly,

compared to the NCO, the reversible discharge capacity (above 4.1 V) is well maintained for the subsequent cycles, and thus, the discharge curves are more superimposed at a potential range higher than 3.25 V during the 100 cycles, unlike the other two samples. This complex voltage behavior becomes more distinguishable in the differential capacity plots of the second charge/discharge curve in Figure 2.4d. NCO exhibits several distinct peaks corresponding to voltage plateaus. As the amount of substituted Ti increases, these peaks become broad.

The effects of Ti substitution on capacity retention are summarized in Figure 2.4e. The initial discharge capacities of $\text{Na}_{0.67}\text{Co}_{1-x}\text{Ti}_x\text{O}_2$ ($x = 0, 0.05, \text{ and } 0.1$) are similar to each other (145.9, 145.0 and 135.0 mAh g^{-1} , respectively). However, as Ti substitution increases, specific capacity decreases, because the substituted Ti^{4+} are inactive for electrochemical cycling. Unlike the behavior of similar initial specific capacities, their cycle lives are very different. Due to the irreversible capacity at the high-potential region and the relatively low-capacity retention of NCO, the discharge capacity of the $\text{Na}_{0.67}\text{Co}_{0.90}\text{Ti}_{0.10}\text{O}_2$ is the highest even after 100 cycles. Thus, the capacity retention of $\text{Na}_{0.67}\text{Co}_{1-x}\text{Ti}_x\text{O}_2$ ($x = 0, 0.05, \text{ and } 0.1$) after 100 cycles is 71.9, 73.2, and 85.5% respectively. After substitution of Ti ions, Coulombic efficiencies during cycling also significantly increase, indicating that the pristine NCO has more irreversible losses, and Ti substitution is effective at reducing such irreversible reactions for subsequent cycles as well as initial cycles.

For calculating the energy density of the prepared materials, the average discharge potentials were obtained (3.01, 3.08, and 3.18 V) for $\text{Na}_{0.67}\text{Co}_{1-x}\text{Ti}_x\text{O}_2$ ($x = 0, 0.05 \text{ and } 0.1$). Ti substitution induces the beneficial effect of high average potential, leading to high energy density. Based on the highest average potential of 0.1 of Ti-

substituted samples, the inclined voltage curves are believed to remain undisturbed by the polarization. Thus, Ti-substituted $\text{Na}_{0.67}\text{Co}_{0.90}\text{Ti}_{0.10}\text{O}_2$ shows higher specific energy than NCO, except for a few initial cycles as shown in Figure 2.4f. The higher specific energy is attributed to reversible high voltage energy and good capacity retention.

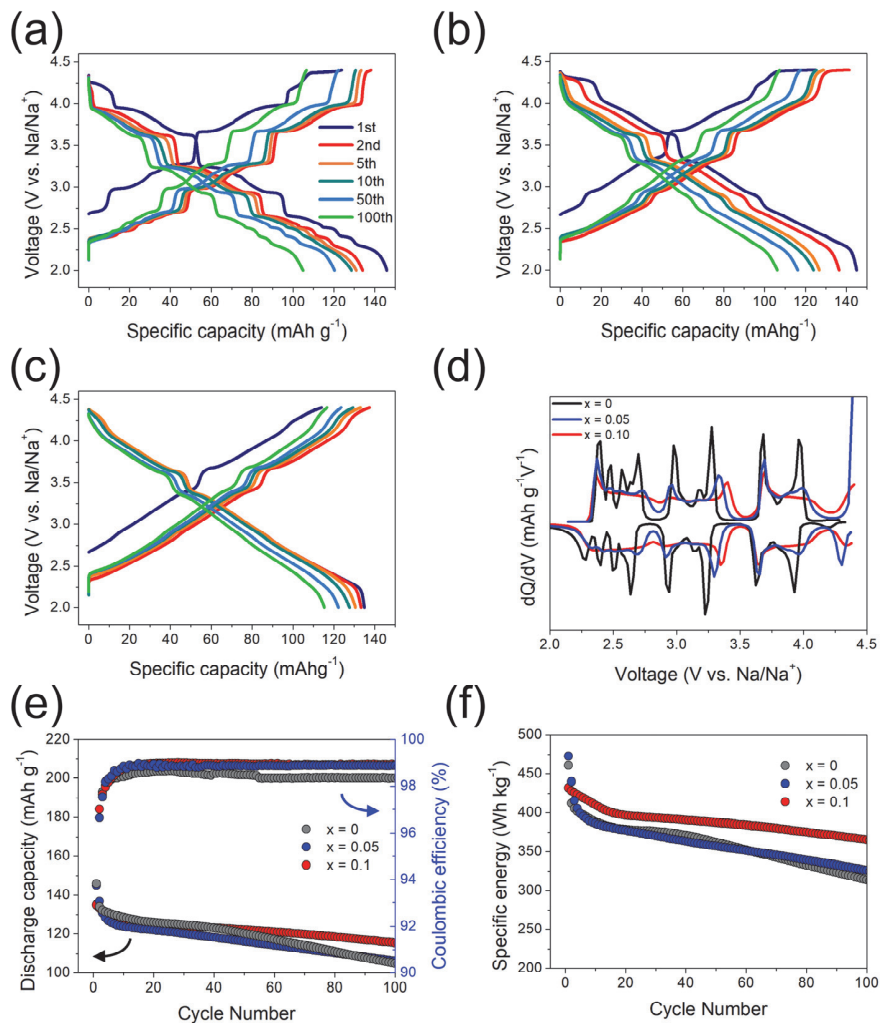


Figure 2. 4 Electrochemical cycling performance of the Na/Na_{0.67}Co_{1-x}Ti_xO₂ ($x = 0, 0.05, \text{ and } 0.1$) cells. (a–c) Galvanostatic charge/discharge curve of Na_{0.67}Co_{1-x}Ti_xO₂ ($x = 0, 0.05, \text{ and } 0.1$) during 100 cycles. The test was conducted at 100 mA g⁻¹ between 2 and 4.4 V. (d) dQ/dV plots of the 2nd charge/discharge curve from a-c. (e) Specific capacity and Coulombic efficiency of each cell as a function of cycle number. (f) Specific energy of each cell as a function of cycle number.

Various current densities were applied to evaluate rate capabilities with the same potential conditions. Figure 2.5a shows discharge capacities of $\text{Na}_{0.67}\text{Co}_{1-x}\text{Ti}_x\text{O}_2$ ($x = 0, 0.05, \text{ and } 0.10$). Up to 200 mA g^{-1} (1.48 C , $1 \text{ C} = 135 \text{ mA g}^{-1}$), they show a similar discharge capacity. At high current densities from 500 mA g^{-1} (3.7 C) to 5000 mA g^{-1} (37 C), the rate capability improves depending on the amount of Ti. As the amount of Ti substitution increases until $x = 0.10$ in $\text{Na}_{0.67}\text{Co}_{1-x}\text{Ti}_x\text{O}_2$, the rate capability greatly improves. In particular, $\text{Na}_{0.67}\text{Co}_{0.90}\text{Ti}_{0.10}\text{O}_2$ has a highly improved rate capability of 65 mAh g^{-1} even under a high current density of 5000 mA g^{-1} , while $\text{Na}_{0.67}\text{CoO}_2$ and $\text{Na}_{0.67}\text{Co}_{0.95}\text{Ti}_{0.05}\text{O}_2$ have capacities of 10 and 34 mAh g^{-1} at the same current density. At the 41st cycle, after the rate capability evaluations, every cell had a similar rebounded capacity of around 120 mAh g^{-1} again under a low current density of 0.1 A g^{-1} . This implies that the improved rate capability is attributed to the relief of kinetic resistance by Ti substitution rather than the disappearance of active sites for Na ions at high-potential conditions over 4.4 V . Figure 2.5b and c shows the voltage curves under various current conditions, which are depicted in Figure 2.5a. Thus, Ti substitution greatly improves the rate capability of NCO in the voltage range between 2 and 4.4 V . This improvement is expected to occur because of the evasion of the Na^+ /vacancy ordering, which acts as activation barrier of Na^+ diffusion.

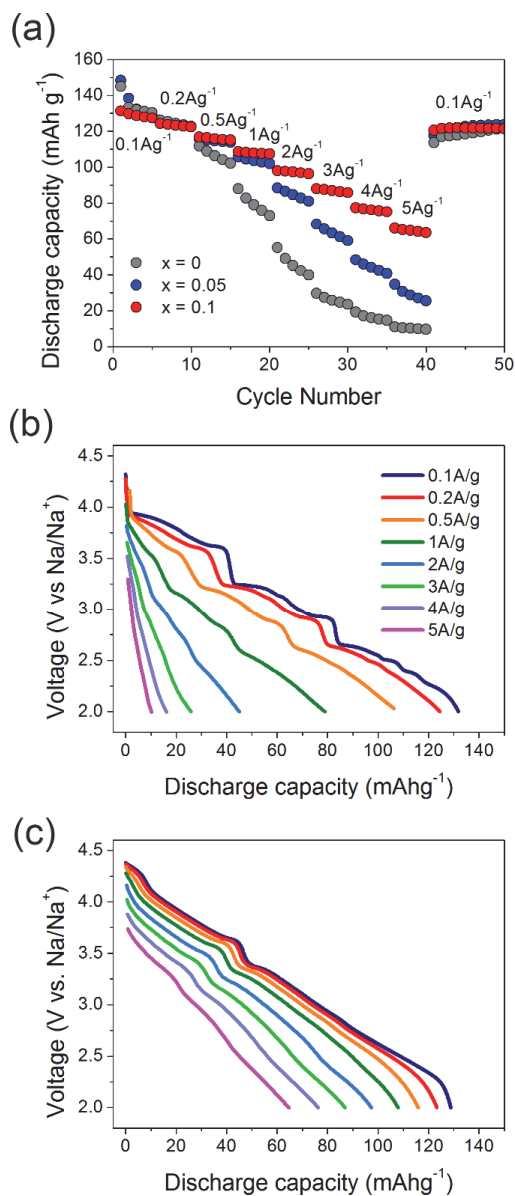


Figure 2. 5 (a) Rate performance of the Na/Na_{0.67}Co_{1-x}Ti_xO₂ ($x = 0, 0.05$ and 0.1) cells. Discharge curves with various current densities for (b) Na_{0.67}CoO₂ and (c) Na_{0.67}Co_{0.90}Ti_{0.10}O₂, respectively.

To investigate the electrochemical behavior in detail, the galvanostatic intermittent titration technique (GITT) was applied to $\text{Na}_{0.67}\text{Co}_{1-x}\text{Ti}_x\text{O}_2$ ($x = 0$ and 0.1), as shown in Figure 2.6. For the first charging sequence under 4 V, the polarization is very low, reflecting high Na diffusion in that potential region. The shape of the voltage curves also highly corresponds to the voltage curves in Figure 2.6a and c, in which NCO has many steps of the first-order transition, and $\text{Na}_{0.67}\text{Co}_{0.90}\text{Ti}_{0.10}\text{O}_2$ has only one plateau at 3.25 V. In that region, no prominent polarization is observed, implying that both materials have a moderate rate of Na^+ diffusion. [39] Considering the polarization behavior, a notable difference appears above 4 V. At potential regions over 4 V ($>105 \text{ mAh g}^{-1}$), polarization higher than 0.2 V is observed in the curve of NCO (Figure 2.6b), and the high polarization is maintained until the completion of charging.

On the contrary, $\text{Na}_{0.67}\text{Co}_{0.90}\text{Ti}_{0.10}\text{O}_2$ shows clearly different reaction pathways above 4 V in terms of polarization. With a relatively small increase in polarization, a sloping curve can be observed at potentials from 4 to 4.4 V. $\text{Na}_{0.67}\text{Co}_{0.90}\text{Ti}_{0.10}\text{O}_2$ exhibits the behavior of a single-phase reaction by mitigated Na^+ /vacancy ordering during the extraction of Na^+ above 4 V. Because its polarization is lower than that of NCO, it can utilize additional Na^+ up to 4.4 V. Meanwhile, the stabilized potential changes in NCO in a highly desodiated state. This observation is more evident in the voltage vs time curve of GITT (Figure 2.6b). The part with increasing voltage is the sequence where the charging current is applied, and the part with decreasing voltage is the remaining section without charge. After charging to 4.36 V with large polarization (the first green arrow in the Figure 2.6b), a voltage drop appears as soon as the rest is applied. The open circuit voltage (OCV) is stabilized at 4.34 V after an

instant voltage drop. Subsequently, the OCV falls deeper below 4.2 V. The highly desodiated NCO over 4 V is believed to be unstable, and a phase change occurs when it is under the rest. This phase change is expected to be the irreversible reaction of NCO above 4 V. This reaction will be discussed further in the following section. Contrary to NCO, over the 4 V region, $\text{Na}_{0.67}\text{Co}_{0.90}\text{Ti}_{0.10}\text{O}_2$ undergoes relaxation immediately after charging (Figure 2.6c) without any voltage drop. In addition, its OCV remains higher than that of NCO. This result shows that $\text{Na}_{0.67}\text{Co}_{0.90}\text{Ti}_{0.10}\text{O}_2$ becomes more stable than NCO by substituting Co with Ti when highly desodiated and does not undergo any phase change.

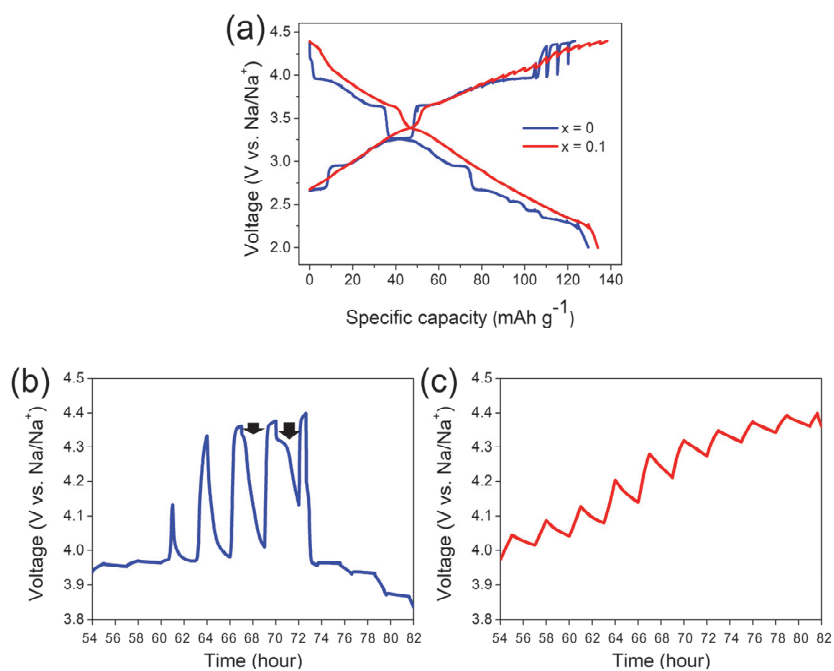


Figure 2. 6 (a) Galvanostatic intermittent titration technique (GITT) curves of Na_{0.67}CoO₂ and Na_{0.67}Co_{0.90}Ti_{0.10}O₂. These GITT curves involve a repeated charge at 5 mA g⁻¹ for 1 h followed by resting for 2 h. Voltage plots as a function of time for (b) Na_{0.67}CoO₂ and (c) Na_{0.67}Co_{0.90}Ti_{0.10}O₂.

To examine the irreversible reaction and effect of Ti substitution, a more severe cutoff condition (2–4.5 V) is intentionally applied. During repeated cycling, NCO undergoes a sharp decrease in reversible capacity, and its value is almost negligible after 100 cycles. On the other hand, even though $\text{Na}_{0.67}\text{Co}_{0.90}\text{Ti}_{0.10}\text{O}_2$ shows a steep decline similar to NCO at the beginning, a stable cycle retention appears after 10 cycles, as shown in Figure 2.7a. Each sample also shows a difference in Coulombic efficiency. $\text{Na}_{0.67}\text{Co}_{0.90}\text{Ti}_{0.10}\text{O}_2$ shows a high Coulombic efficiency of 99% along cycles, but NCO has an average Coulombic efficiency of 91%, implying that a severe irreversible reaction occurs. Figure 2.7b and c shows charge/discharge curves of NCO and $\text{Na}_{0.67}\text{Co}_{0.90}\text{Ti}_{0.10}\text{O}_2$, respectively. During the first charge process, a plateau appears at 4.375 V for NCO, and its initial charge and discharge capacity is 130.8 and 149.0 mAh g^{-1} , respectively. After the first cycle, the charge plateau at 4.375 V disappears, and the discharge capacity of NCO dramatically decreases to 130.5 mAh g^{-1} with large polarization. After 100 cycles, the reversible capacity of NCO becomes almost zero owing to high polarization. For $\text{Na}_{0.67}\text{Co}_{0.90}\text{Ti}_{0.10}\text{O}_2$, no charge plateau exists at 2.0–4.4 V, but it appears at 4.43 V during the first charge process. Its initial charge and discharge capacities are 150.9 and 167.2 mAh g^{-1} , which are higher than those of NCO under the same conditions. Similar to NCO, $\text{Na}_{0.67}\text{Co}_{0.90}\text{Ti}_{0.10}\text{O}_2$ shows a polarization increase and a capacity fading after the first cycle. However, after 10 cycles, it shows much more stable cycle retention. In particular, it has 114 mAh g^{-1} after 100 cycles, whereas NCO has a negligible specific capacity at the same cycle number (Figure 2.7a).

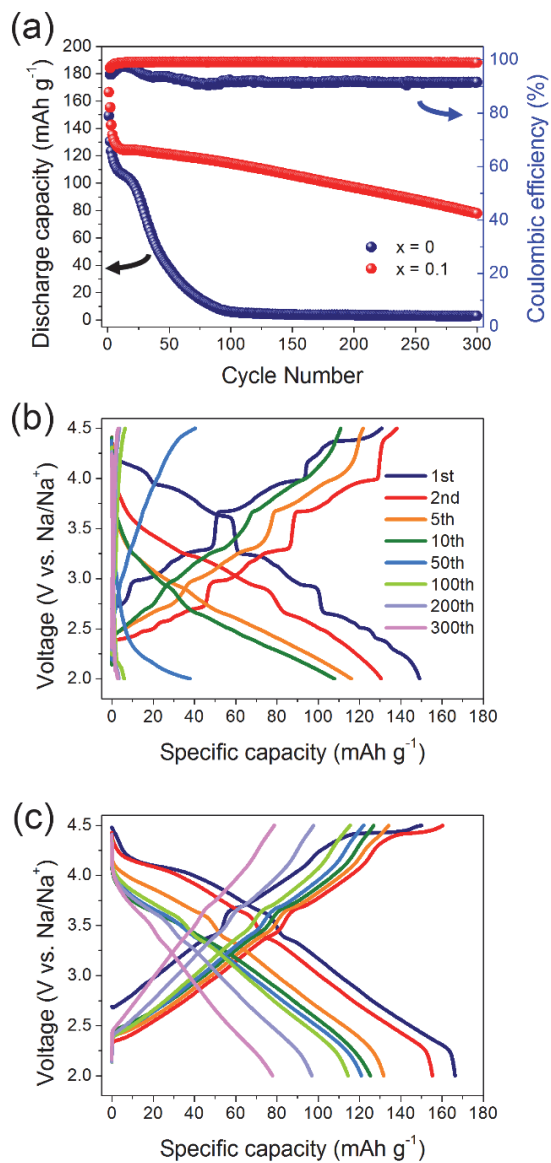


Figure 2. 7 Electrochemical cycling performance of the Na/Na_{0.67}Co_{1-x}Ti_xO₂ ($x = 0$ and 0.1) cells, where 100 mA g⁻¹ of current density is applied between 2.0 and 4.5 V. (a) Discharge capacity and Coulombic efficiency of each cell as a function of cycle number up to 300 cycles. (b,c) Charge/discharge curves of Na_{0.67}CoO₂ and Na_{0.67}Co_{0.90}Ti_{0.10}O₂, respectively.

To identify structural changes after the capacity decay of NCO when cycled up to 4.5 V, XRD analysis was performed for the NCO electrode after 300 cycles of charge/discharge with various cutoff values (Figure 2.8). XRD patterns of the long cycled sample and a sample discharged at 2.0 V immediately after cell assembly were analyzed. However, no peak was found for the impurity phase except for the peak shift by the state of charge (SOC). Therefore, the major reason for the poor cyclability is not bulk structure changes but kinetic hindrances of surface resistance. This can be confirmed by electrochemistry (Figure 2.9). After the capacity decay, NCO recovered 83% of initial discharge capacity when a low current density (2 mA g⁻¹) was applied. Because XRD analysis is not sensitive to surface analysis, TEM SAED analysis was additionally performed to investigate the surface of Na_{0.67}CoO₂ after capacity decay caused by charging to 4.5 V, as shown in Figure 2.10.

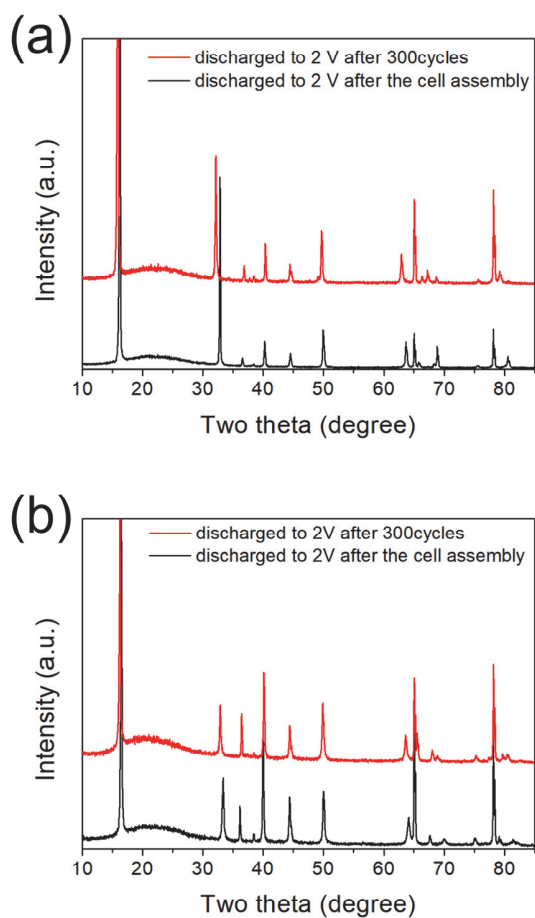


Figure 2. 8 Ex situ XRD patterns of (a) $\text{Na}_{0.67}\text{CoO}_2$ and (b) $\text{Na}_{0.67}\text{Co}_{0.90}\text{Ti}_{0.10}\text{O}_2$. For each sample, an electrode discharged after cell assembly and an electrode discharge after 300 cycles were compared.

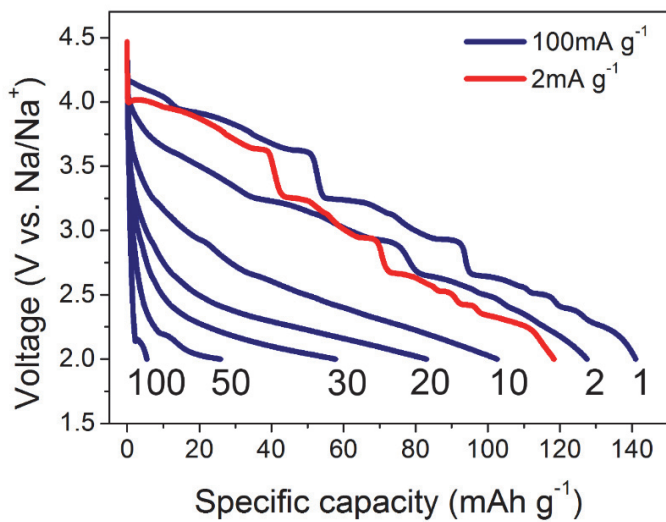


Figure 2. 9 Discharge profile of $\text{Na}_{0.67}\text{CoO}_2$ at a very low current density (2 mA g^{-1}) after 100 charge/discharge cycling in a voltage window 2-4.5 V at 100 mA g^{-1} .

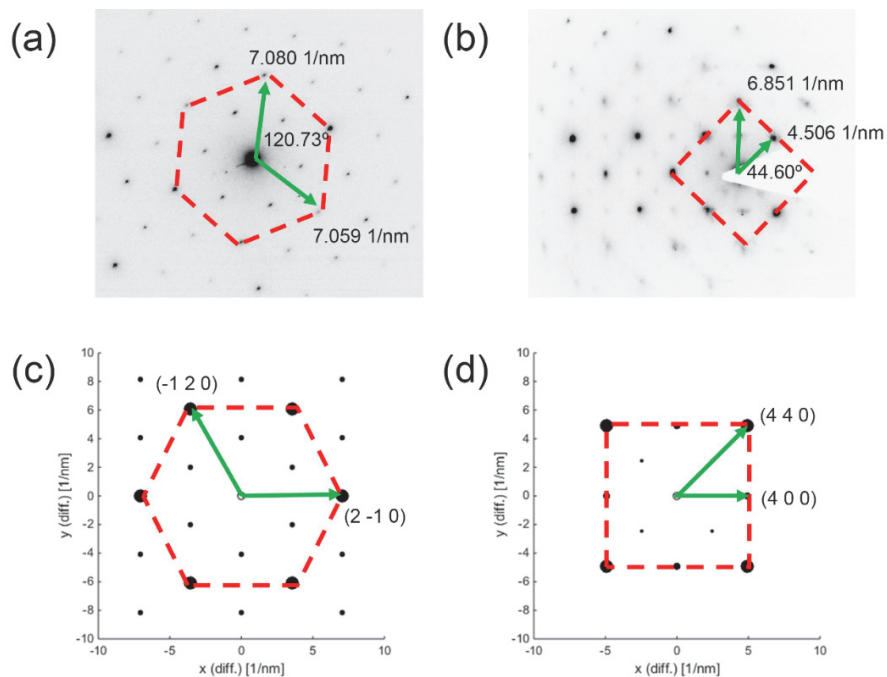
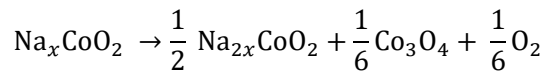


Figure 2. 10 (a),(b) Two different TEM SAED patterns observed from the surface of capacity decayed $\text{Na}_{0.67}\text{CoO}_2$ (after 100 cycles between 2.0 and 4.5 V). (c) Simulated SAED pattern of a zone axis $[0\ 0\ 1]$ of Na_xCoO_2 . (d) Simulated SAED pattern of a zone axis $[1\ 0\ 0]$ of Co_3O_4 .

From the TEM SAED analysis, not only hexagonal NCO but also cubic Co_3O_4 was clearly detected at the particle surface as shown in Figure 2.10a and b, respectively. Figure 2.10c and d shows calculated the SAED patterns of NCO with a $[0\ 0\ 1]$ zone axis and Co_3O_4 with a $[1\ 0\ 0]$ zone axis as obtained by CrystBox software. [40] The real patterns are almost identical to the calculated patterns. Unlike NCO, $\text{Na}_{0.67}\text{Co}_{0.90}\text{Ti}_{0.10}\text{O}_2$ exhibits only a hexagonal $[0\ 0\ 1]$ SAED pattern at particle surfaces (Figure 2.11). The Co_3O_4 phase is expected as the side product of the irreversible reaction at a high voltage, which causes capacity decay. Similar to previous reports on the capacity decay of the Li analogue, LiCoO_2 , impedance growth by Co_3O_4 is expected to occur at the surface. [41] The formation of Co_3O_4 through a reaction between P2-type $\text{Na}_{0.67}\text{CoO}_2$ and the electrolyte at a high temperature (ARC test) was reported by Dahn *et al.* [42] The reaction is expressed as below



The above reaction is also expected to be accelerated by an electrochemical side reaction with the electrolyte or the electrode when a high voltage (≥ 4.4 V) is applied. [43] The difference between the two reactions is that, in electrochemical reactions, passivation by Co_3O_4 limits the reaction to the surface, but under heating conditions, the reaction occurs not only at the surface but also in the bulk such that it becomes detectable by XRD. As shown above, this Co_3O_4 formation involves the discharge of electrode and oxygen evolution.

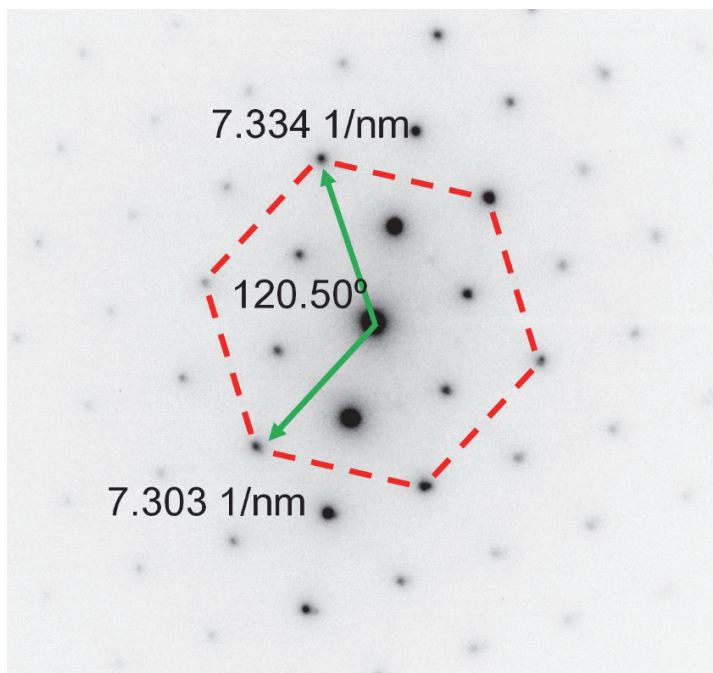


Figure 2. 11 TEM SAED patterns observed from the surface of $\text{Na}_{0.67}\text{Co}_{0.90}\text{Ti}_{0.10}\text{O}_2$ after 100cycles between 2.0-4.5 V.

To further investigate the irreversible reactions associated with the Co_3O_4 formation, transmission in situ XRD analysis was performed. Figure 2.12a and b shows the obtained voltage curves of NCO and $\text{Na}_{0.67}\text{Co}_{0.90}\text{Ti}_{0.10}\text{O}_2$ during in situ XRD measurements. In the right side of Figure 2.12a and b, the (002) peak shift of $\text{Na}_{0.67}\text{CoO}_2$ (Figure 2.12a) and $\text{Na}_{0.67}\text{Co}_{0.90}\text{Ti}_{0.10}\text{O}_2$ (Figure 2.12b) are depicted. The lattice parameter of c corresponding to each peak is marked in Figure 2.12c. This is directly related to the sodium content in the electrode. The lattice parameter c values of $\text{Na}_{0.67}\text{Co}_{0.90}\text{Ti}_{0.10}\text{O}_2$ appear to be larger than those of $\text{Na}_{0.67}\text{CoO}_2$ throughout the charge and the rest process. As sodium ions are extracted from both electrodes, the value of lattice parameter c gradually increases up to ~ 4 V, because a repulsive interaction between oxygen planes grows. After the increase, differences in the lattice parameter behavior occur between $\text{Na}_{0.67}\text{CoO}_2$ and $\text{Na}_{0.67}\text{Co}_{0.90}\text{Ti}_{0.10}\text{O}_2$. For $\text{Na}_{0.67}\text{Co}_{0.90}\text{Ti}_{0.10}\text{O}_2$, a nearly constant c value is maintained until the end of charge, continuing even to the following rest stage. However, for NCO, the c value is similarly maintained as the charge continues but abruptly decreases as the voltage curve reaches higher than 4.0 V ($0.2 > x$ mole of Na in the form of Na_xCoO_2). This shows that unfavorable changes in the crystal structure occur beyond 4.0 V for NCO. Nevertheless, this problematic behavior is significantly mitigated by Ti substitution as shown in Figure 2.12c.

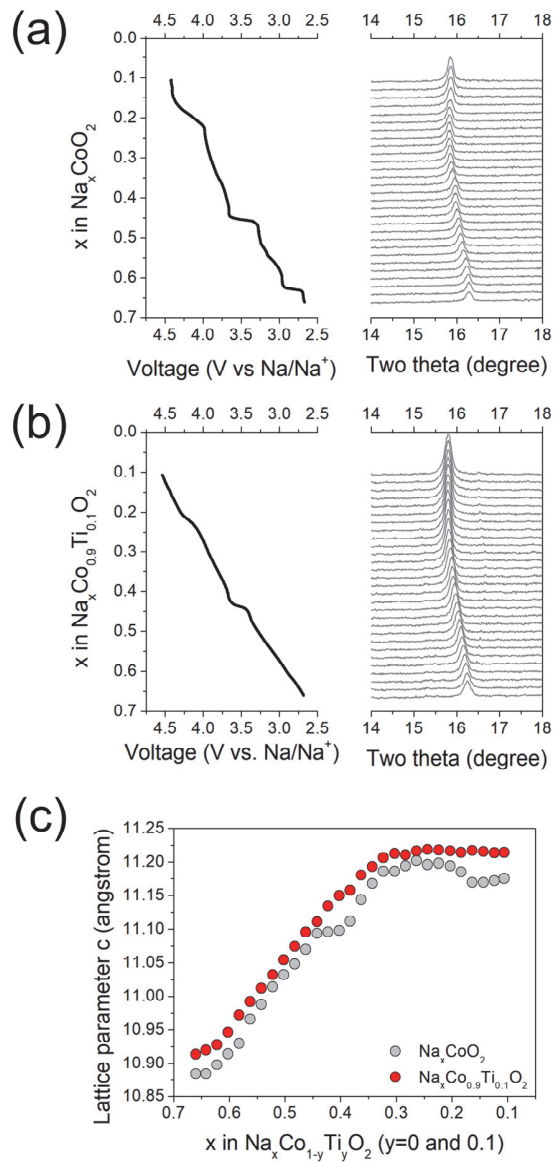


Figure 2. 12 Transmission in situ XRD patterns (right side) with voltage profiles (left side) of (a) $\text{Na}_{0.67}\text{CoO}_2$ and (b) $\text{Na}_{0.67}\text{Co}_{0.90}\text{Ti}_{0.10}\text{O}_2$ during galvanostatic charging at a rate of 10 mA g^{-1} . The peak is a hexagonal (0 0 2) peak. (c) Evolution of lattice parameter c for $\text{Na}_{0.67}\text{CoO}_2$ and $\text{Na}_{0.67}\text{Co}_{0.90}\text{Ti}_{0.10}\text{O}_2$ according to Na content.

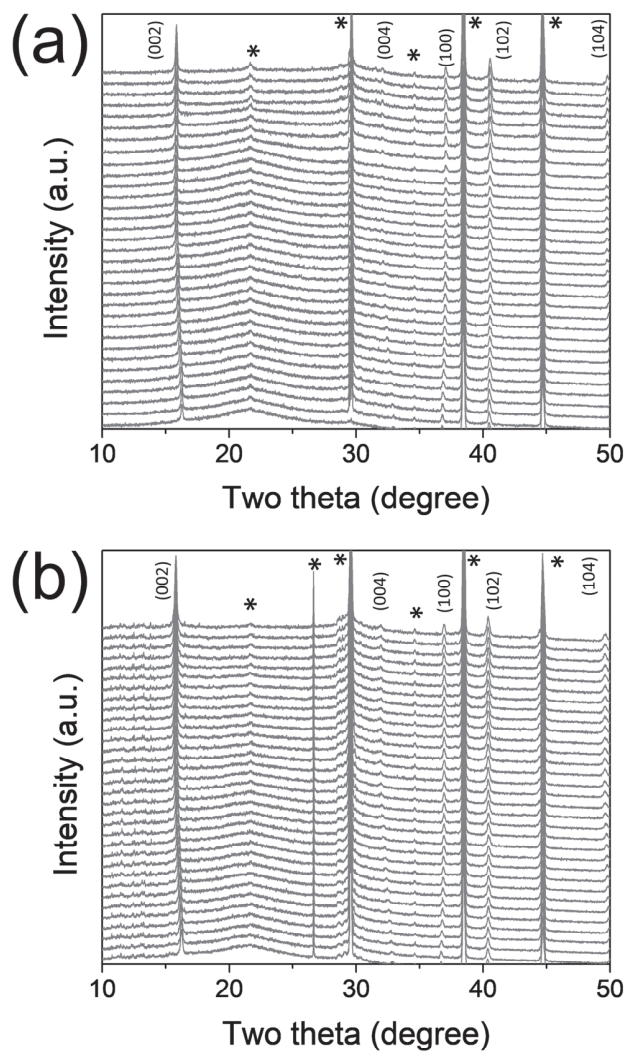


Figure 2. 13 Transmission in situ XRD analysis of (a) $\text{Na}_{0.67}\text{CoO}_2$ and (b) $\text{Na}_{0.67}\text{Co}_{0.90}\text{Ti}_{0.10}\text{O}_2$ from 10 to 50° during the first charge. Peaks with asterisk are diffraction peaks of in situ cell parts.

When Ti ions substitute a part of Co ions in NCO, the tendency of the irreversible reaction occurring at high voltage is significantly reduced. This is due to the following two factors. For the irreversible reaction to occur, disproportionation of Co ions ($2\text{Co}^{3+} \rightarrow \text{Co}^{2+} + \text{Co}^{4+}$) and oxygen evolution ($\text{O}^{2-} \rightarrow 1/2\text{O}_2 + 2\text{e}^-$) must occur. In the above-mentioned cycleability in Figure 2.7a, Ti substitution effectively reduces the irreversible reaction in the above two aspects. First, disproportionation of Co^{3+} ions occurs via charge transfer between two Co^{3+} ions. Substitution of Ti^{4+} reduces the possibility of Co^{3+} pair formation. Because Ti ions are less electronegative than Co ions, charge transfer from Co to Ti is inhibited. When Ti is substituted, the formation probability of Co^{3+} pair is reduced. Second, Ti ions are more ionic in the bonding with oxygen. Therefore, it is more difficult for oxygen to break away from the bonding with the metal ion when Ti is substituted. Irreversible reactions in the Ti-substituted sample occur at a higher voltage (4.425 V) than in the case of early stages (4.375 V) at the same current density. Furthermore, it maintains a more stable phase under high voltage. Consequently, Ti-substituted $\text{Na}_x\text{Co}_{0.90}\text{Ti}_{0.10}\text{O}_2$ resists phase transformation that occurs at high voltages and shows superior cycle stability than pristine NCO.

2.3. Conclusions

In this study, we demonstrated the effect of Ti substitution on P2-type Na_xCoO_2 through electrochemical analyses, TEM SAED, and transmission in situ XRD analysis. Various types of P2- $\text{Na}_{0.67}\text{Co}_{1-x}\text{Ti}_x\text{O}_2$ ($x = 0, 0.05, 0.1, 0.15,$ and 0.2) were synthesized via solid-state synthesis. Among these, P2- $\text{Na}_{0.67}\text{Co}_{1-x}\text{Ti}_x\text{O}_2$, with an amount of Ti ions higher than $x = 0.1$, develops an unfavorable second crystal structure. Ti substitution effectively mitigated Na^+ /vacancy ordering in the P2-type Na_xCoO_2 , as the amount of Ti increases showing smooth voltage profiles. In particular, $\text{Na}_x\text{Co}_{0.90}\text{Ti}_{0.10}\text{O}_2$ shows small increases in polarization even at over 4 V, which is contrary to the sharp increase in the polarization of Na_xCoO_2 . These results show that Ti-substituted $\text{Na}_{0.67}\text{Co}_{0.90}\text{Ti}_{0.10}\text{O}_2$ can be used in developing cells with long cyclability even under high cutoff potential. Naturally, $\text{Na}_{0.67}\text{Co}_{0.90}\text{Ti}_{0.10}\text{O}_2$ has higher specific energy than pristine $\text{Na}_{0.67}\text{CoO}_2$. The rate capabilities of the P2-type $\text{Na}_{0.67}\text{Co}_{1-x}\text{Ti}_x\text{O}_2$ ($x = 0, 0.05,$ and 0.1) are effectively enhanced as the amount of Ti increases. In the case of pristine $\text{Na}_{0.67}\text{CoO}_2$, Co_3O_4 formation occurs on the surface at high voltage, leading to severe capacity degradation. However, Ti-substituted $\text{Na}_{0.67}\text{Co}_{0.90}\text{Ti}_{0.10}\text{O}_2$ is much more stable and can withstand over 100 mAh g^{-1} of discharge capacity after 150 cycles and maintain a cycle life over 300 cycles with 4.5 V of high cutoff because of its stronger bonding. Our research highlights that the energy density of sodium layered oxide materials can be increased with enhanced electrochemical stability by controlling Na^+ /vacancy ordering through chemical substitution.

2.4. Experimental section

2.4.1. Materials Synthesis

P2-type $\text{Na}_{0.67}\text{Co}_{1-x}\text{Ti}_x\text{O}_2$ ($x = 0, 0.05, 0.1, 0.15$ and 0.2) was synthesized by a solid-state reaction. Na_2CO_3 (Kanto Chemical), Co_3O_4 (Alfa Aesar), and TiO_2 (Sigma-Aldrich) powders were used as starting materials. Excess Na_2CO_3 of 10 wt.% was used for compensating the loss of sodium during heat treatment because of its high volatility. The powders were homogeneously mixed via ball milling with acetone as a liquid medium followed by drying at 65°C overnight. The mixture powders were pressed into a pellet was and then heated in air at 900°C for 20 h. When the pellet was quenched to room temperature, it was transferred to an argon-filled glovebox to avoid unfavorable reactions with ambient atmosphere and moisture.

2.4.2. Structural Analysis

Synchrotron X-ray powder diffraction (SXRPD) patterns were obtained at the 9B HRPD beamline of the Pohang Light Source II in the Republic of Korea. The incident beam was vertically collimated using a mirror and monochromatized to a wavelength of 1.49150 \AA using a double-crystal Si (111) monochromator. To minimize the preferred orientation effects, a rotating sample holder was used during scanning. Diffraction patterns were collected in the 2θ scan mode with a step size of 0.01° from 10 to 130° . To refine the structure using the Rietveld method, the EXPGUI program, which is a graphical user interface of the General Structure Analysis System (GSAS), was used. [44] Inductively coupled plasma atomic emission spectroscopy (ICP-AES) was performed to obtain the atomic composition of each sample using an OPTIMA 8300 (PerkinElmer, U.S.A.). Field emission

scanning electron microscopy (FESEM) images were collected using the MERLIN Compact (Zeiss, Germany). The SAED pattern of Na_xCoO_2 with capacity decay after 100 cycles between 2.0 and 4.5 V was obtained using Tecnai F20 (FEI, U.S.A.).

2.4.3. Electrochemical Method

P2-type $\text{Na}_{0.67}\text{Co}_{1-x}\text{Ti}_x\text{O}_2$ ($x = 0, 0.05, 0.1, \text{ and } 0.15$) slurries were prepared by mixing active material powders, Super P, and poly vinylidene fluoride (PVDF) in N-methylpyrrolidone (NMP) (Sigma-Aldrich) with a weight ratio of 8:1:1. These homogeneously mixed slurries were cast onto Al foil and subsequently dried at 60 °C for 2 h in vacuum. The dried foils were roll-pressed and dried at 120 °C in a vacuum for 8 h again before being used as a positive electrode. For the electrochemical tests, CR2032-type coin cells were assembled in the argon-filled glove box. Sodium metal (Sigma-Aldrich) was used as the negative electrode, and 1 M NaClO_4 in ethylenecarbonate/propylenecarbonate (1:1 v/v) with 5 wt. % FEC as an additive was used as the electrolyte. A glass fiber (Whatman GF-A) was used as a separator. Electrochemical tests were performed using a WBCS3000S (WonAtech, Korea) at 25 °C

2.4.4. Transmission in Situ XRD Analysis

To apply transmission in situ XRD analysis, a customized coin cell with a hole in the center and Al mesh electrode was used to reduce interference of Al substrate. In situ XRD patterns were collected using Smartlab (Rigaku, Japan) with $\text{Cu K}\alpha$ radiation (1.5406 Å). Each cell was charged at a current density of 10 mA g^{-1} for 13 h and then rested for 2 h. An XRD pattern was obtained at intervals of about 28 min.

2.4.5 Electrochemical characterization of materials

Electrodes were made by mixing the 70 wt% of active material, 15 wt% of super P and 15 wt% of poly (acrylic acid) in *n*-methyl-2-pyrrolidinone. Afterwards, the slurries were dried in a vacuum oven overnight. Sodium metal was used as the counter electrode, while a glass fiber GF/C (Whatman) and 1.0 M NaClO₄ in ethylene carbonate (EC)/propylene carbonate (PC) (1:1 by volume) were used as the separator and the electrolyte, respectively. In addition, 5wt% fluoroethylene carbonate (FEC) was added to the electrolyte as an additive. The loading levels of the active materials were 1 mg cm⁻². 2032-type coin cells were assembled in an Ar-filled glove box and tested using a WBCS3000 cycler (WanATech) in the range from 0.01 V to 3.0 V (vs. Na⁺/Na) at 25 °C.

2.5. References

- [1] M. Armand, J. M. Tarascon, *Nature*, **2008**, 451, 652.
- [2] N. S. Choi, Z. Chen, S. A. Freunberger, X. Ji, Y. K. Sun, K. Amine, G. Yushin, L. F. Nazar, J. Cho, P. G. Bruce, *Angew. Chem. Int. Ed.*, **2012**, 51, 9994.
- [3] J. M. Tarascon, *Nat. Chem.*, **2010**, 2, 510.
- [4] L. P. Wang, L. Yu, X. Wang, M. Srinivasan, Z. J. Xu, *J. Mater. Chem. A*, **2015**, 3, 9353.
- [5] H. Kim, H. Kim, Z. Ding, M. H. Lee, K. Lim, G. Yoon, K. Kang, *Adv. Energy Mater.*, **2016**, 6, 1600943.
- [6] N. Yabuuchi, K. Kubota, M. Dahbi, S. Komaba, *Chem. Rev.*, **2014**, 114, 11636-11682.
- [7] M. D. Slater, D. Kim, E. Lee, C. S. Johnson, *Adv. Funct. Mater.*, **2013**, 23, 947.
- [8] J.-Y. Hwang, S.-T. Myung, Y.-K. Sun, *Chem. Soc. Rev.*, **2017**, 46, 3529.
- [9] Y. H. Liao, K. S. Park, P. H. Xiao, G. Henkelman, W. S. Li, J. B. Goodenough, *Chem. Mater.*, **2013**, 25, 1699.
- [10] S. Komaba, C. Takei, T. Nakayama, A. Ogata, N. Yabuuchi, *Electrochem. Commun.*, **2010**, 12, 355.
- [11] C. Didier, M. Guignard, C. Denage, O. Szajwaj, S. Ito, I. Saadoune, J. Darriet, C. Delmas, *Electrochem. Solid-State Lett.*, **2011**, 14, A75.
- [12] X. H. Ma, H. L. Chen, G. Ceder, *J. Electrochem. Soc.*, **2011**, 158, A1307.
- [13] P. Vassilaras, X. H. Ma, X. Li, G. Ceder, *J. Electrochem. Soc.*, **2013**, 160, A207.
- [14] Y. Bai, L. Zhao, C. Wu, H. Li, F. Wu, *ACS Appl. Mater. Interfaces*, **2016**, 8, 2857.
- [15] M.-S. Kwon, S. G. Lim, Y. Park, S.-M. Lee, K. Y. Chung, T. J. Shin, K. T. Lee,

- ACS Appl. Mater. Interfaces*, **2017**, *9*, 14758.
- [16] C. Delmas, C. Fouassier, P. Hagenmuller, *Physica B+C*, **1980**, *99*, 81.
- [17] C. Delmas, J. J. Braconnier, C. Fouassier, P. Hagenmuller, *Solid State Ionics*, **1981**, *3-4*, 165.
- [18] R. Berthelot, D. Carlier, C. Delmas, *Nat. Mater.*, **2011**, *10*, 74.
- [19] M. Roger, D. J. Morris, D. A. Tennant, M. J. Gutmann, J. P. Goff, J. U. Hoffmann, R. Feyerherm, E. Dudzik, D. Prabhakaran, A. T. Boothroyd, N. Shannon, B. Lake, P. P. Deen, *Nature*, **2007**, *445*, 631.
- [20] A. J. Toumar, S. P. Ong, W. D. Richards, S. Dacek, G. Ceder, *Phys. Rev. Applied*, **2015**, *4*, 064002.
- [21] X. Li, X. Ma, D. Su, L. Liu, R. Chisnell, S. P. Ong, H. Chen, A. Toumar, J. C. Idrobo, Y. Lei, J. Bai, F. Wang, J. W. Lynn, Y. S. Lee, G. Ceder, *Nat. Mater.*, **2014**, *13*, 586.
- [22] Z. Lu, J. R. Dahn, *J. Electrochem. Soc.*, **2001**, *148*, A1225.
- [23] C. Didier, M. Guignard, J. Darriet, C. Delmas, *Inorg. Chem.*, **2012**, *51*, 11007.
- [24] M. Guignard, C. Didier, J. Darriet, P. Bordet, E. Elkaim, C. Delmas, *Nat. Mater.*, **2013**, *12*, 74.
- [25] G. J. Shu, F. C. Chou, *Phys. Rev. B: Condens. Matter Mater. Phys.*, **2008**, *78*, 052101.
- [26] D. H. Lee, J. Xu, Y. S. Meng, *Phys. Chem. Chem. Phys.*, **2013**, *15*, 3304.
- [27] B. Mortemard de Boisse, D. Carlier, M. Guignard, L. Bourgeois, C. Delmas, *Inorg. Chem.*, **2014**, *53*, 11197.
- [28] Y. Wang, R. Xiao, Y. S. Hu, M. Avdeev, L. Chen, *Nat. Commun.*, **2015**, *6*, 6954.
- [29] Y. Tsuchiya, K. Takanashi, T. Nishinobo, A. Hokura, M. Yonemura, T.

- Matsukawa, T. Ishigaki, K. Yamanaka, T. Ohta, N. Yabuuchi, *Chem. Mater.*, **2016**, 28, 7006.
- [30] H. Yoshida, N. Yabuuchi, S. Komaba, *Electrochem. Commun.*, **2013**, 34, 60.
- [31] N. Bucher, S. Hartung, J. B. Franklin, A. M. Wise, L. Y. Lim, H.-Y. Chen, J. N. Weker, M. F. Toney, M. Srinivasan, *Chem. Mater.*, **2016**, 28, 2041.
- [32] N., Sabi, A. Sarapulova, S. Indris, H. Ehrenberg, J. Alami, I. Saadoune, *ACS Appl. Mater. Interfaces*, **2017**, 9, 37778.
- [33] P.-F. Wang, H.-R. Yao, X.-Y. Liu, Y.-X. Yin, J.-N. Zhang, Y. Wen, X. Yu, L. Gu, Y.-G. Guo, *Sci. Adv.*, **2018**, 4, eaar6018.
- [34] J. J. Ding, Y. N. Zhou, Q. Sun, X. Q. Yu, X. Q. Yang, Z. W. Fu, *Electrochim. Acta*, **2013**, 87, 388.
- [35] M. D'Arienzo, R. Ruffo, R. Scotti, F. Morazzoni, C. M. Mari, S. Polizzi, *Phys. Chem. Chem. Phys.*, **2012**, 14, 5945.
- [36] Y. J. Fang, X. Y. Yu, X. W. Lou, *Angew. Chem. Int. Ed.*, **2017**, 56, 5801.
- [37] D. Baster, W. Maziarz, K. Świerczek, A. Stokłosa, J. Molenda, *J. Solid State Electr.*, **2015**, 19, 3605.
- [38] S. H. Guo, Y. Sun, J. Yi, K. Zhu, P. Liu, Y. B. Zhu, G. Z. Zhu, M. W. Chen, M. Ishida, H. S. Zhou, *NPG Asia Mater.*, **2018**, 8, e266.
- [39] T. Shibata, Y. Fukuzumi, W. Kobayashi, Y. Moritomo, *Sci. Rep.*, **2015**, 5, 9006.
- [40] M. Klinger, A. Jager, *J. Appl. Crystallogr.*, **2015**, 48, 2012.
- [41] R. Yazami, Y. Ozawa, H. Gabrisch, B. Fultz, *Electrochim. Acta*, **2004**, 50, 385.
- [42] X. Xia, J. R. Dahn, *J. Electrochem. Soc.*, **2012**, 159, A647.
- [43] S. Hwang, Y. Lee, E. Jo, K. Y. Chung, W. Choi, S. M. Kim, W. Chang, *ACS Appl. Mater. Interfaces*, **2017**, 9, 18883.

[44] B. H, Toby, *J. Appl. Crystallogr.*, **2001**, 34, 210.

국 문 초 록

리튬 이온 배터리는 1991년 상용화 이후 기존 배터리에 비해 높은 작동 전압과 에너지 밀도를 바탕으로 노트북이나 휴대폰 등 소형 제품의 에너지 저장 장치로 널리 사용되었다. 최근 들어 지구온난화와 같은 환경 문제가 국제적으로 대두됨에 따라 전기자동차 및 그리드 용 에너지 저장 장치 등 대규모 에너지 저장 장치에 대한 수요가 크게 증가하였다. 이러한 상황 속에서 리튬 자원은 그 분포가 제한적이며 매장량 또한 많지 않아 수요 상승에 따른 가격 상승이 리튬 이온 배터리의 대량 공급에 리스크로 작용할 수 있다. 이러한 배경으로부터 대용량 에너지 저장 장치를 위한 다양한 리튬 이온 배터리 대체재들에 대한 연구가 현재 활발하게 이루어지고 있다.

이러한 대체재 중 소듐 이온 배터리는 리튬 이온 배터리의 전하 전달체(charge carrier)인 리튬을 소듐으로 대체한 것으로서 리튬 자원에 비해 소듐 자원은 비용적 이점이 있으며 매장량도 풍부해 리튬 이온 배터리가 가진 리튬 자원의 리스크가 없다는 장점이 있다. 따라서, 소듐의 비용적 이점을 살려 대용량 저장 장치에 소듐 이온 배터리를 적용하고자 하는 연구가 활발하다. 하지만 소듐은 리튬에 비해 크기가 크고 무거우며 표준환원전위가 높아 상대적으로 낮은 에너지 밀도를 갖는다. 그러므로 소듐 이온 배터리의 성공적인 상용화를 위해서는 높은 에너지 밀도를 갖는 전극 재료의 개발이 핵심이라고 할 수 있다. 특히, 양극 재료는 소듐 이온 배터리의 전압을 결정하는 역할을 하므로, 높은 전압을 가진 재

료의 개발이 매우 필요하다고 할 수 있다.

먼저, 1장에서는 소듐 이온 전지에 대하여 간략하게 소개 한다. 특히, 전하전달체인 소듐을 리튬과 비교하여 소듐 이온 배터리가 어떠한 장, 단점을 가지는 지에 대해 설명하였다. 그리고 소듐 이온 배터리에서 가장 에너지 밀도가 높은 물질 군인 P2-타입 층상구조 양극 물질에 대해 두 가지 재료를 예로 들어서 설명하였다. 마지막으로, 2장에서 주요한 변수로서 작용하는 3가지 오더링 (ordering)에 대해서 설명하였다.

2장에서는 P2-타입 소듐 코발트 산화물 (P2-type $\text{Na}_{0.67}\text{CoO}_2$)에 Ti 치환을 통해 소듐 베이컨시 오더링 ($\text{Na}^+/\text{vacancy}$ ordering)을 완화시키고 나아가 상 변이가 억제되는 것을 이용하여 작동전압영역을 확대하였다. 일반적으로 층상구조 물질은 높은 전압 영역에서 비가역적인 상 변이로 가용한 전하량에 한계가 있다. 하지만 Ti 치환을 통해 소듐 베이컨시 오더링이 완화된 P2-타입 소듐 코발트 티타늄 산화물 (P2-type $\text{Na}_{0.67}\text{Co}_{0.90}\text{Ti}_{0.10}\text{O}_2$) 에서는 높은 전압 영역까지 상 변이가 나타나지 않아 기존보다 작동 전압 영역을 향상시킬 수 있었으며 이에 따라 에너지 밀도도 향상하게 되었다. 기존의 소듐 베이컨시 오더링을 억제하는 연구는 율속 특성 (rate capability)을 향상시키는 데 중점을 두고 있었으나 이번 연구를 통해 소듐 베이컨시 오더링을 통한 상 변이 완화가 에너지 밀도 향상에도 기여할 수 있다는 가능성을 확인하였다.

주요어: 소듐 이온 배터리, 층상구조 양극 물질, 양이온 배열, 가역성, 고전압

학 번: 2014-22589